



Sulfur- and Iron-Rich Mineralogical Features Preserved in Permafrost in the Canadian High Arctic: Analogs for the Astrobiological Exploration of Mars

Graham E. Lau^{1,2*}, Christopher B. Trivedi^{3,4}, Stephen E. Grasby⁵, John R. Spear³, Julie Cosmidis^{1,6} and Alexis S. Templeton^{1*}

¹Department of Geological Sciences, University of Colorado Boulder, Boulder, CO, United States, ²Blue Marble Space Institute of Science, Seattle, WA, United States, ³Department of Civil and Environmental Engineering, Colorado School of Mines, Golden, CO, United States, ⁴Interface Geochemistry, GFZ German Research Centre for Geosciences, Potsdam, Germany, ⁵Geological Survey of Canada, Calgary, AB, Canada, ⁶Department of Earth Sciences, University of Oxford, Oxford, United Kingdom

OPEN ACCESS

Edited by:

Margarita Safonova,
Indian Institute of Astrophysics, India

Reviewed by:

Luis Gago-Duport,
University of Vigo, Spain
Christian Schröder,
University of Stirling, United Kingdom

*Correspondence:

Graham E. Lau
grahamlau@bmsis.org
Alexis S. Templeton
alexis.templeton@colorado.edu

Specialty section:

This article was submitted to
Astrobiology,
a section of the journal
Frontiers in Astronomy and Space
Sciences

Received: 29 November 2021

Accepted: 21 March 2022

Published: 07 April 2022

Citation:

Lau GE, Trivedi CB, Grasby SE,
Spear JR, Cosmidis J and
Templeton AS (2022) Sulfur- and Iron-
Rich Mineralogical Features Preserved
in Permafrost in the Canadian High
Arctic: Analogs for the Astrobiological
Exploration of Mars.
Front. Astron. Space Sci. 9:825019.
doi: 10.3389/fspas.2022.825019

Elliptical sulfate-rich features, stained red by the presence of iron oxides, are set within permafrost and carbonate rock at Borup Fiord Pass in the Canadian High Arctic. These features, which vary in diameter from ~0.5 to 3 m, exhibit the co-localization of sulfur (S) and iron (Fe) minerals, with S and Fe both preserved in multiple oxidation states. Through application of x-ray diffraction (XRD) and Raman microspectroscopy, we find that these features appear to encapsulate central cores with abundant pyrite while S⁰, gypsum, and iron-bearing secondary minerals such as jarosite, goethite, and hematite have formed from oxidative weathering of the pyrite. These features appear similar to terrestrial gossans, mineral features representative of weathered sulfide ores in the near-surface. We use Raman microspectroscopy and scanning transmission x-ray microscopy (STXM) to show that organic carbon is associated with the minerals within these features. The origin of this carbon remains enigmatic; however, we consider the possibility that this carbon, along with etching of the pyrite grains and accumulation of encrusted filaments detected in the features, may be indicative of preserved biological activity during alteration of the pyrite. We also consider how such geological sulfide emplacements and their weathered surface expressions may provide a target for future surface and remote sensing studies of Mars and in the search for extraterrestrial life.

Keywords: sulfur minerals, pyrite alteration, gossan, Arctic, Mars, astrobiological

INTRODUCTION

Pyrite is the most common metal sulfide mineral at the Earth's surface (e.g., Rickard and Luther, 2007), and can form through multiple pathways. These include precipitation within magmatic and volcanic/hydrothermal systems as well as through biologically driven processes in anoxic, low-temperature sulfidic systems. Sulfide ore deposits formed directly from magmatic sources, where sulfides are essentially smelted from intrusive magmas, often consist of pyrrhotite, pentlandite, and chalcopyrite (Barnes et al., 2017), while hydrothermal deposits can be enriched in pyrite and other sulfide minerals as well (Fontboté et al., 2017). Meanwhile, sedimentary pyrite emplacements are

common in myriad environments on Earth and constitute some 95% or more of the sulfide on the surface of our planet (Bottrell et al., 2006; Rickard, 2012; Rickard et al., 2017). Furthermore, the majority of this pyrite in sedimentary deposits is formed through biological sulfate reduction (BSR) and subsequent titration of geologically available ferrous iron (Picard et al., 2016; Rickard et al., 2017). Such pyrite deposits form a critical record of the evolution of the global biogeochemical sulfur cycle on Earth (Canfield, 2001; Canfield and Farquhar, 2012).

The acidic weathering of minerals in pyrite-rich, near-surface systems can produce recognizable alteration mineral assemblages and creates gradients of chemical disequilibrium that provide habitable, though perhaps relatively extreme, environments for life (e.g., Edwards et al., 1999; Edwards et al., 2000a; Zolotov and Shock, 2005; Amils et al., 2007; Amils, 2016). For instance, the energy available from the oxidation of ferrous iron and sulfur within sulfide minerals to form sulfates, ferric (oxyhydr)oxides, and acidity is harnessed by organisms in a variety of systems on Earth, including acid mine/rock drainage systems like those at Iron Mountain, CA, USA (e.g., Edwards et al., 1999; Edwards et al., 2000a) and the Rio Tinto system in Spain (e.g., Fernández-Remolar et al., 2005; Amils et al., 2007; Amils, 2016). Furthermore, the oxidative leaching of pyrite in near-surface veins forms geological structures known as gossans. Gossans produce recognizable, stratified alteration features, with circular red staining from iron oxides often overlying the region of the sulfide vein. Also known as “red caps,” gossans have long been a target for ore exploration (e.g., Taylor and Eggleton, 2001; West et al., 2009; Percival and Williamson, 2016).

Terrestrial systems with sedimentary pyrite emplacements, as well as the products of the acidic alteration of such pyrite, are important analogs for our explorations of potentially inhabited (or, at least, habitable) environments on Mars. Biological formation and/or alteration of Fe-S minerals produces mineral assemblages that are diagnostic of biological activity on Earth and so could be a target for exploring potential signs of past or present life on Mars. Iron and sulfur are both enriched in the Martian crust (e.g., Toulmin et al., 1977; Gellert and Clark, 2015), and the formation and weathering of iron sulfide deposits may be a key piece to understanding iron and sulfur mineralogy in Mars’ surface and near-surface environments (Burns and Fisher, 1990a; Wallace et al., 1994; Peretyazhko et al., 2021). Though limited in detection thus far, reduced sulfur and iron sulfide minerals (such as pyrrhotite and pyrite) have been observed and/or inferred on Mars through rover-based instrumentation (Morris et al., 2008; Vaniman et al., 2014; Rampe et al., 2017; Wong et al., 2020), while sulfates have been identified globally through remote sensing (Ehlmann and Edwards, 2014) and observed directly in many locations on the surface (e.g., Squyres et al., 2004; Nachon et al., 2014; Rapin et al., 2016). Although undetected to-date, gossans or similar pyrite- and/or sulfide-alteration features may exist within the Martian near-surface and may have provided environments for life on the Red Planet (Burns, 1987; Burns and Fisher, 1990a).

Conspicuous red-stained features rich in iron and sulfur that are embedded in surrounding carbonate rock and permafrost have been observed at Borup Fiord Pass in the Canadian High

Arctic and may serve as potential analogs for similar systems should they be detected on Mars. These features occur in a valley that has been of astrobiological interest due to the presence of a modern, sulfide-rich, biologically-active spring system at a nearby glacier (Grasby et al., 2003; Gleeson et al., 2010; Gleeson et al., 2011; Wright et al., 2013; Lau et al., 2017; Trivedi et al., 2020). It is not currently known if the hydrogeochemical system driving the modern-day springs is related to the red-stained features in the valley, though Grasby et al. (2012) have implicated the features as remnants of past spring features.

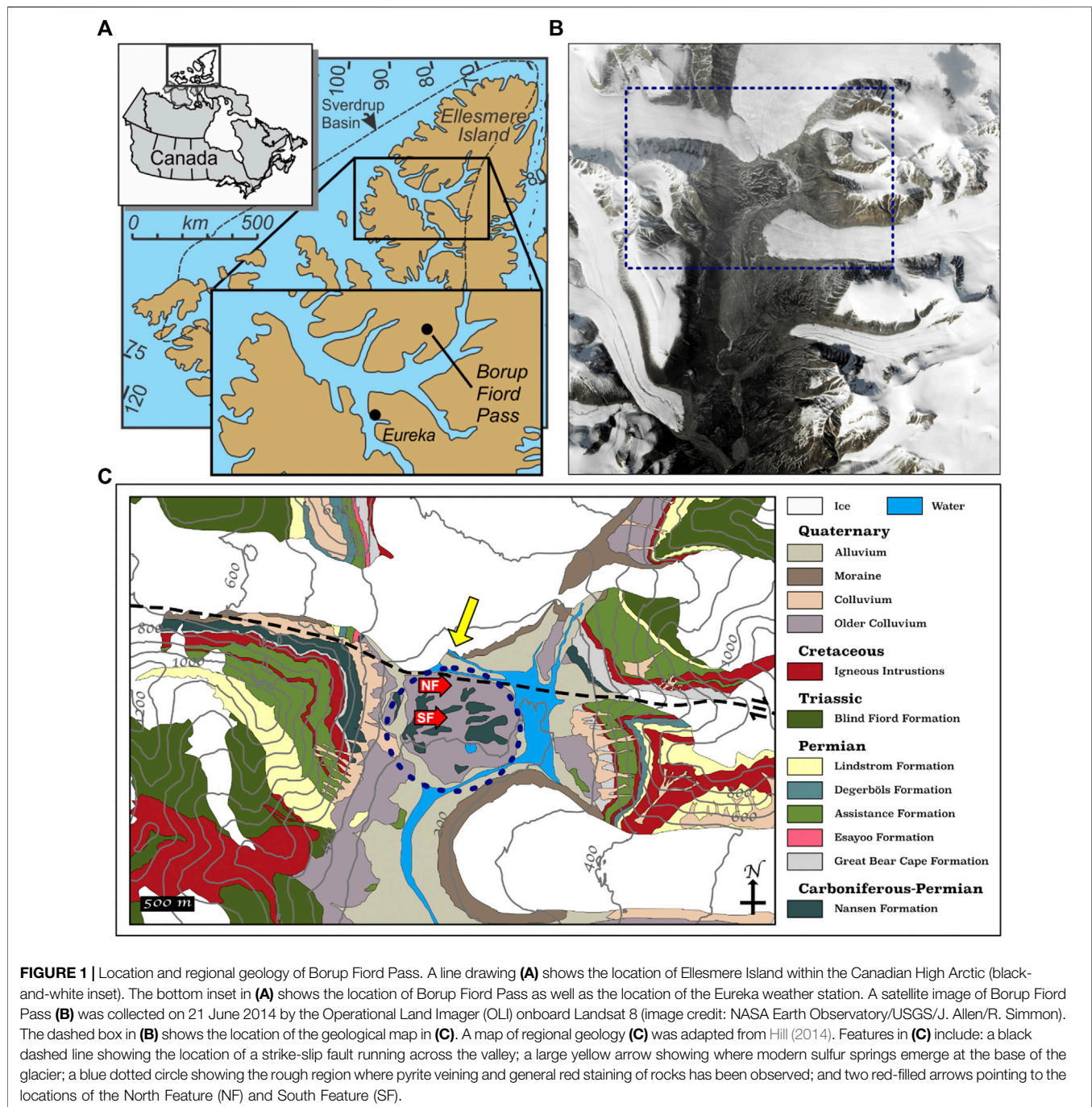
In this work, we set out to intensively characterize the red-stained mineral features at Borup Fiord Pass. Using geochemical and spectroscopic methods, including x-ray diffraction (XRD), Raman microspectroscopy, scanning electron microscopy (SEM), and scanning transmission x-ray microscopy (STXM), we detail the bulk and microscale mineralogy of two of the features. Furthermore, we examine these features for their relevance to Mars exploration and evaluate whether they represent an example of a habitable environment that could be produced and preserved within Fe-S rich mineral deposits on Earth, Mars, and beyond.

MATERIALS AND METHODS

Field Site and Sample Collection

Borup Fiord Pass is a north-south trending valley located at ~81°N, 81°W, on Ellesmere Island in the Canadian High Arctic (Figure 1). The geology of this region was first described in scientific writing by Thorsteinsson and Tozer (1957), with further characterization of the valley’s stratigraphy reported by Gleeson et al. (2011) and Hill (2014). Borup Fiord Pass occurs within the Krieger Mountains, in the deformed eastern portion of the Sverdrup Sedimentary Basin, a Carboniferous to Eocene depocenter (Embry and Beauchamp, 2008). The valley’s surface is composed primarily of Carboniferous to Permian carbonate units. A right-lateral strike-slip fault crosses this valley roughly 100 m from the toe of a coalescence glacier (“Borup Fiord Pass Glacier”), which forms from the merger of local alpine glaciers (Grasby et al., 2003; Gleeson et al., 2011). Modern-day sulfide-rich springs and spring derived ices (aufeis) form at the toe of this glacier and have been the focus of previous research due to the presence of extensive deposits of elemental sulfur that form at this site (Grasby et al., 2003; Gleeson et al., 2012; Wright et al., 2013; Trivedi et al., 2018; Trivedi et al., 2020). The valley where these sulfur deposits and the red-stained mineral features are located in a polar desert region, with mean annual rainfall <100 mm and mean annual air temperatures of -19.7°C as reported at the Eureka meteorological station ~140 km to the southwest (Figure 1A; Grasby et al., 2003).

Materials for this study were collected during a summer field campaign in 2014. Two of the conspicuous red-stained features were selected for surface sampling (Figure 1C), one of which was also selected for subsurface sampling (Figure 2). For subsurface samples, a trench was dug by shovel to provide access to near-surface materials (Figures 2C,D). Three samples were collected from ~30 cm below the surface from the side wall of this trench. In addition, a core drill was used to collect material from the



permafrost-hosted material below the trench (which had been dug until permafrost hindered hand-powered action, at ~60 cm below the surface). Cores of material were wrapped in aluminum foil and placed on ice during transport back to the laboratory (the core material did not maintain a cylindrical structure, instead breaking apart upon warming once removed from the subsurface). Other samples were collected using plastic bags and sterile polyethylene tubes and were stored at ambient temperatures during transport. After transport to the laboratory, all materials were stored at -70°C until analysis.

The feature in **Figure 2A** is located to the north, near the fault crossing the valley and so was named “North Feature” (NF). Samples from this structure are called NF1, NF2, and NF3. The other feature (**Figures 2B,C**) is located ~400 m to the south of the fault and so is here called “South Feature” (SF). Samples from this feature are named relative to their position in the shovel-dug trench: samples of material from the top of the trench before digging are named T1 and T2 (for the top material from the center and rim of the trench, respectively); samples from the side wall of the trench are labeled S1, S2, and S3; and samples of core

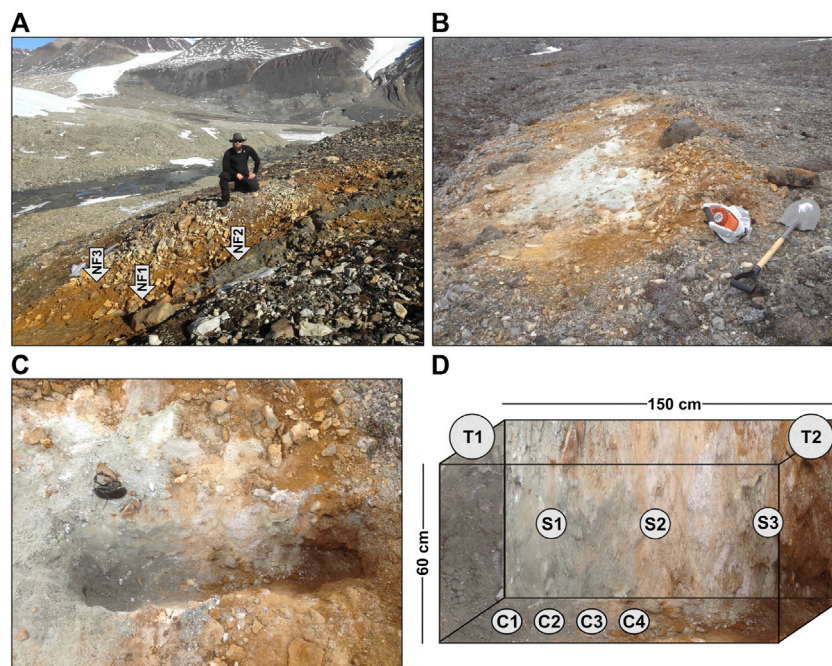


FIGURE 2 | Mineral alteration features and sampling locations. Samples were collected from the features labeled as North Feature (NF; **A**) and South Feature (SF; **B**). Samples NF1, NF2, and NF3 are labeled in **(A)** (with author GL for scale). For site SF, a shovel and core drill (shown in **B**) were used to dig a trench and take samples from the permafrost **(C)**. Goggles are shown in **(C)** for scale. The locations of samples collected from this feature are shown in a representation of the trench in **(D)**. Sample names from the trench samples are included. Approximate lengths along the long axes of the features in **(A)** and **(B)** are 4 m.

material extracted from below the trench are labeled C1 through C4 (all labels in respective positions within the trench are shown in **Figure 2D**).

Total Organic Carbon Measurement

Samples for total organic carbon (TOC) analysis were prepared by repeat washing with concentrated (1 M) HCl to remove carbonate carbon followed by centrifugation and removal of supernatants. TOC measurements were made in the Arikaree Environmental Laboratory (AEL) at the Institute for Arctic and Alpine Research (INSTAAR) at the University of Colorado Boulder using a FLASH EA 1112 Series CHN Analyzer (Thermo Finnigan, LLC., San Jose, CA, USA). Data were calibrated using an atropine standard.

Isotopic Measurements

Isotopes of sulfur (^{32}S and ^{34}S) were analyzed through elemental analyzer isotope ratio mass spectrometry (EA-IRMS) in the Isotope Science Laboratory at the University of Calgary. $\delta^{34}\text{S}$ values were standardized against V-CDT (Vienna Canyon Diablo Troilite). Sulfur isotopes were measured in sulfides and sulfates from submitted samples. Sulfide was first extracted through washing of material with acidified water and then sieving to select reflective grains greater than $425\ \mu\text{m}$. Sulfates were extracted from samples by the Isotope Science Laboratory prior to analysis.

X-Ray Diffraction

X-ray diffraction (XRD) data were collected on either a D2 PHASER desktop diffractometer (Bruker Corporation;

Billerica, MA, USA) at the University of Colorado Boulder or a D500 diffractometer (Siemens AG, Berlin, Germany) at the United States Geological Survey (USGS). X-rays were generated as Cu K α radiation and data were collected with 1- to 2-s dwell times per step and steps of $0.02^\circ 2\theta$. Ranges of data collection vary for some samples, but all cover at least 15° – $60^\circ 2\theta$. Prior to data collection, samples were dried and then ground to a fine powder. Samples were packed on Si-wafers for reduced background and rotated during data collection to reduce common orientation effects. XRD patterns were analyzed using Jade 9 (Materials Data Inc., Livermore, CA, USA) and the JCPDS PDF-2 database, 2001 release (ICDD: Newtown Square, PA, USA, 2001).

Raman Spectroscopy

Raman microspectroscopy of samples was performed at the University of Colorado Boulder using a LabRAM HR Evolution Raman spectrometer (Horiba, Ltd., Kyoto, Japan) with reflected light microscopy for imaging and a 532 nm green laser for Raman spectroscopy. Data collection and analysis was conducted using Horiba's LabSpec 6 (v6.4.1.63) spectroscopy suite. Raman spectra were processed using LabSpec and peaks were fit with reference compounds from the RRUFF database (Lafuente et al., 2015), either manually or by using the program Know-It-All (Bio-Rad Laboratories, Hercules, CA, USA). Spectral maps were processed using LabSpec and were corrected using the Instrument Correction System (ICS) process and then subtracted to baselines using 3rd degree polynomial functions applied over 100+ data points. Noise

points were added into baselines with low signal data. Map data were analyzed using the classical least squares (CLS) and multivariate curve resolution (MCR) applications within LabSpec to spatially resolve components within map regions and to detect the range of components within map data.

Electron Microscopy

Material for scanning electron microscopy (SEM) was thoroughly dried and then placed on carbon tape over an aluminum stud. Samples were sputter coated with Au to decrease charging artifacts. Electron microscopy was conducted at the Nanomaterials Characterization Facility (NCF) at the University of Colorado Boulder using a JEOL JSM-6480LV SEM outfitted with an energy dispersive spectroscopy (EDS) x-ray detector. SEM was conducted in secondary electron mode with accelerating voltages from 2 to 5 kV for imaging and 15 kV for EDS.

X-Ray Microscopy

Scanning transmission x-ray microscopy (STXM) was conducted at the sulfur L-edge and carbon K-edge at the soft x-ray spectromicroscopy (SM) beamline, 10ID-1, at the Canadian Lightsource (CLS) in Saskatoon, Saskatchewan, Canada. STXM was used to map the distribution and characterize the speciation of sulfur and carbon in the sample at a 35 nm spatial resolution. STXM data were collected on samples which were prepared through repeated washings with ultrapure water to remove salts. Samples were then mixed with ultrapure water and allowed to settle. Supernatants were then sampled with micropipettes and deposited on gold carbon-coated TEM grids. Material was thoroughly dried before analysis. The sample was then placed in a vacuum chamber for STXM collection; the chamber was evacuated to ~13 Pa and then back-filled with He to standard atmospheric pressure before data acquisition. The monochromator was calibrated using the standard 3p Rydberg transition of gaseous CO₂ at 294.96 eV. Scanning transmission x-ray images were collected for sulfur at four energies (160, 163, 170, and 173 eV). These energies were selected to target variations in x-ray transmission intensities for reduced and oxidized sulfur compounds (160 vs. 163 eV and 170 vs. 173 eV, respectively; e.g., Jalilehvand, 2006). For carbon, images were collected at 280.0 eV (below the C K-edge) and 288.2 eV (the absorption energy of 1s→π* electronic transitions of carbon in amide groups; Benzerara et al., 2004). Maps were then collected over energies correlating with the S L-edge (155–190 eV) and the C K-edge (260–340 eV) using step sizes ranging from 0.114 to 10 eV (smaller step sizes were selected over the ranges of interest for sulfur and carbon compounds while large step sizes were used in regions where only baseline data would be collected; **Supplementary Table S1**). STXM data were processed using the aXis2000 software package (Hitchcock, 2015). Transmission intensity data for images were converted to optical densities (OD). The differences in OD between images at the energy of interest and below the edge were used to generate maps of sulfur and organic carbon distribution within sample materials. These maps were then used to select regions for collections of stacks of images over ranges of energies through

either the sulfur L-edge (155–190 eV) or the carbon K-edge (260–340 eV). X-ray absorption near edge structure (XANES) spectra were generated from image stacks using aXis 2000. Linear background corrections were applied to the spectra below the C K-edge and the S L-edge to eliminate the contributions of lower energy absorption edges. The spectra were compared to the literature for speciation interpretations.

RESULTS

Field Observations and Sampling

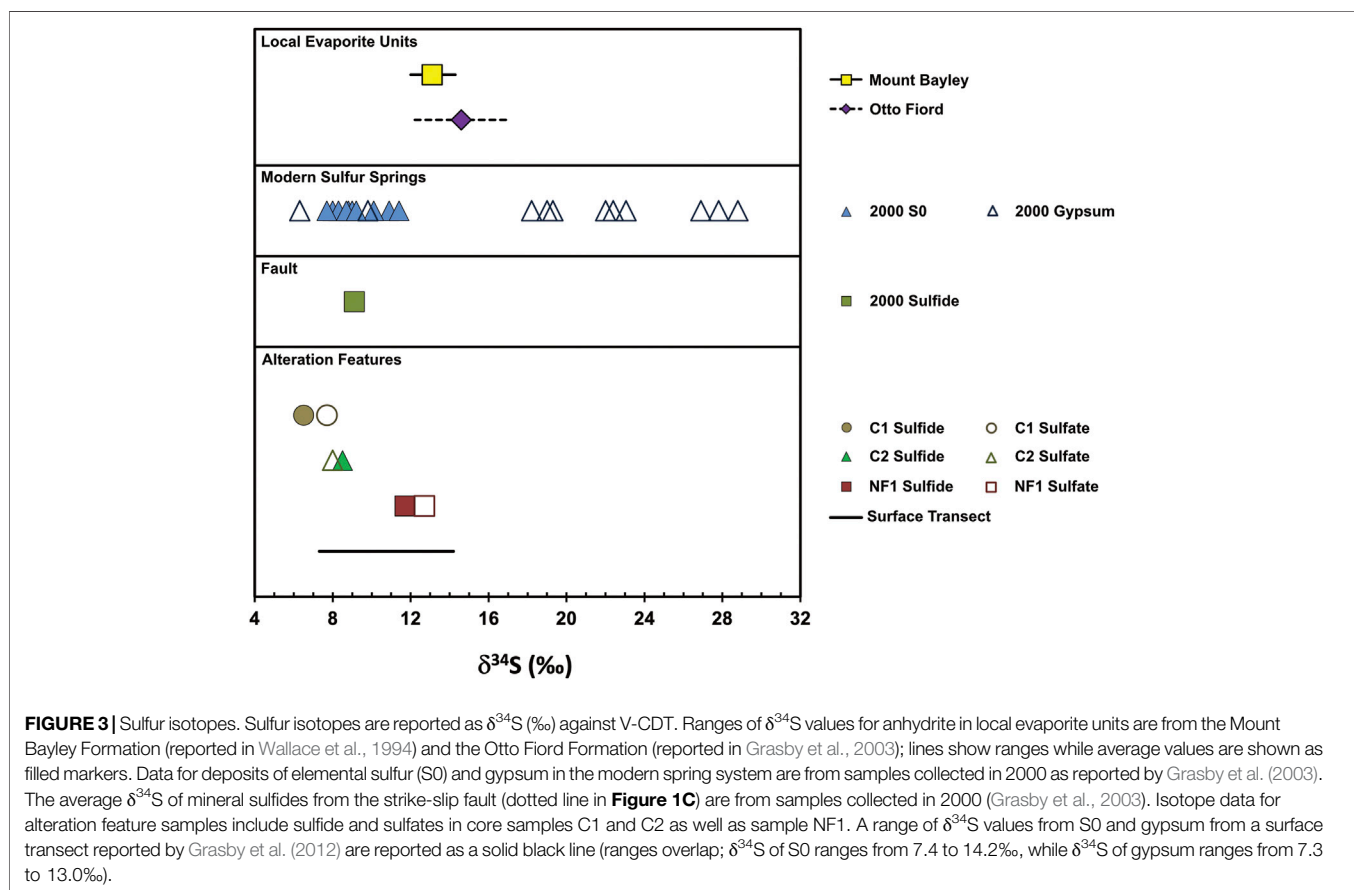
The red-stained rocks at Borup Fiord Pass are located on a hill, standing ~50 m above the surrounding valley and having a diameter of ~1,000 m (**Figure 1C**; **Supplementary Figures S1–S3**). This topographically high region lies just to the south of a strike-slip fault that crosses the valley. Previous mapping in this region revealed that the exposed materials on this hill are mostly Quaternary glacial deposits and exposed limestone rock of the Permian-aged Nansen Formation (Grasby et al., 2003; Hill, 2014; **Figure 1**). Six red-stained elliptical features have been identified on this hill to-date, with two of these revealing white-colored central regions (**Supplementary Figure S2**). While the feature labeled NF lies along the fault at the north end of the hill, the other features all occur ~400 m to the south and lie within ~50 m from each other. The red-stained features stand out against the grey carbonate rocks of the surrounding valley (**Figure 2**; **Supplementary Figure S3**). The material within the features is crystalline, but also friable. All of the elliptical features are 1–5 m in diameter and show apparent red staining from the presence of iron oxides (measured here and in previous work). Also, abundant red staining of rocks can be observed in areas around the hill where the features are located. For instance, a small lake (which can be seen in satellite imagery; **Supplementary Figure S1**) roughly 100 m from most of the features has abundant red-stained rocks (**Supplementary Figure S3**). In addition, to the west of the alteration features on the hill is a drainage, informally referred to as “pyrite canyon”, where carbonate rocks are marked by veins of pyrite (identified visually; **Supplementary Figures S1–S3**).

The feature labeled SF in this work, where materials were collected from a trench that was dug into the feature, is the same one that was used for surface mineralogy characterization in a previous study by Grasby et al. (2012). Materials collected in this study as well as in Grasby et al. (2012) appear to show a surface redox gradient moving laterally from the central gypsum- and pyrite-rich region outward through the more iron oxide-rich region. However, these materials in the active zone above the permafrost of the valley may not be entirely representative of the subsurface mineralogy of the features (due to constant exposure to the atmosphere and annual freeze-thaw cycles). For this reason, in the current work, we sampled from the surface as well as from deeper within the active zone and from the permafrost layer below for this feature. Sampling from multiple depths into the structure provided a spatially resolved suite of samples for chemical and mineralogical analyses.

TABLE 1 | Total organic carbon measurements and minerals detected with XRD and Raman spectroscopy.

Sample	TOC (%)	XRD mineralogy	Raman spectroscopic results	
			Common	Less common
T1	0.02	Gypsum, S ⁰ , (pyrite)	Gypsum, pyrite, S ⁰ , OC	Anatase
T2	0.37	Quartz, gypsum, goethite	Goethite, gypsum	OC, anatase, quartz
S1	0.01	Gypsum, S ⁰ , pyrite, anhydrite	Gypsum, S ⁰ , pyrite	OC
S2	0.06	Gypsum, (pyrite)	Gypsum, pyrite, goethite	S ⁰ , OC
S3	0.02	Gypsum, S ⁰ , anhydrite	S ⁰ , gypsum, OC	
C1	DL	Gypsum, pyrite, S ⁰	Pyrite, gypsum, anhydrite, S ⁰ , quartz	OC, calcite, hematite, (silicon)
C2	DL	Gypsum	Gypsum, pyrite, S ⁰ , anhydrite, hematite, iron oxides	Goethite, OC, anatase
C3	DL	Gypsum, (pyrite)	Gypsum, anhydrite, pyrite, S ⁰ , OC	Hematite, mackinawite
C4	DL	Pyrite, gypsum, quartz, S ⁰	Gypsum, pyrite	S ⁰ , OC
NF1	0.19	Gypsum, quartz, jarosite	Gypsum, goethite, jarosite, pyrite, OC	Anatase, quartz
NF2	NM	Gypsum, quartz, pyrite	Gypsum, pyrite, goethite, jarosite, OC	S ⁰
NF3	NM	Gypsum, goethite, quartz, jarosite	Gypsum, goethite, jarosite, quartz, OC	Pyrite, anatase

For TOC measurements, "DL" indicates below detection level of the instrument (see text), while "NM" indicates where no measurement was collected. XRD data are ordered by dominant peak heights; questionable mineral assignments are indicated in parentheses. Raman spectroscopic results are split into the most common and less common phases observed (most common are observed in nearly every observed region of the sample material, while less common phases are sparsely located within the materials). S⁰ indicates elemental sulfur, while OC indicates organic carbon.



Geochemical Measurements and Bulk Mineralogy

Discrete samples taken from core to rim in the alteration features were analyzed to determine total organic carbon content. One sample, T2 from the rim of SF, exhibited a relatively high total

organic carbon (TOC) concentration of 0.37%, while the average TOC over all the remaining measured samples that could be measured was only 0.03% (Table 1). All of the core samples were below the detection limit for the instrument (<0.01% TOC). TOC in samples NF2 and NF3 has not been measured.

X-ray diffraction (XRD) was used to probe the bulk mineralogy of sample materials. XRD data show that gypsum is the primary component of nearly all bulk powder samples, by relative XRD peak heights (Table 1). XRD data for samples T1, S1, C1, and C4 all reveal pyrite, elemental sulfur, and gypsum co-occurring. Quartz was identified in several samples (T2, C4, NF1, NF2, and NF3). Jarosite was detected in NF1 and NF3, but not in any samples from the trench. X-ray diffractograms for each sample are available in the **Supplementary Information**.

Sulfur isotopes ($\delta^{34}\text{S}$) in sulfides and sulfates were measured for three samples. Core samples C1 and C2 from site SF were analyzed to reveal sulfur isotope values of materials preserved within the permafrost. $\delta^{34}\text{S}$ values in sulfides from these samples are 6.5 and 8.5‰, respectively, while $\delta^{34}\text{S}$ in sulfates are 7.7 and 8.0‰, respectively. One sample from site NF (NF1) was measured as well, with a sulfide $\delta^{34}\text{S}$ value of 11.7‰ and sulfate $\delta^{34}\text{S}$ of 12.7‰. These isotopic values are compared to data for other sulfur-bearing materials from Borup Fiord Pass in Figure 3. For instance, a sample from this study that was collected from the fault in the eastern portion of the valley, far from the region of the alteration features, revealed $\delta^{34}\text{S}$ of 16.2‰ in sulfide and 15.2‰ in sulfate. Figure 3 also shows relevant sulfur isotope measurements from Borup Fiord Pass from previous studies. These include $\delta^{34}\text{S}$ values for S^0 and gypsum in the modern spring system sampled in 2,000 and previously reported by Grasby et al. (2003), values for S^0 and gypsum at the surface of site SF as reported by Grasby et al. (2012), pyrite within the fault (Grasby et al., 2003), and $\delta^{34}\text{S}$ measurements for local anhydrite-bearing geological units. These anhydrite-bearing units, such as the Otto Fiord Formation and the Mount Bayley Formation, are proposed to be potential sources of subsurface dissolved sulfate; they have average $\delta^{34}\text{S}$ values of 14.6 and 13.1‰, respectively (Davies and Nassichuk, 1975; Wallace et al., 1994; Grasby et al., 2003).

Raman Microspectroscopy

Raman microspectroscopy allows for spectroscopic identification of the most common mineral phases while also allowing for more spatially resolved analyses that can reveal the discrete spots containing less-common materials within complex samples. Also, while XRD patterns are dominated by the most abundant and crystalline phases, some compounds are more or less Raman active (or not at all), and so Raman spectroscopy can be very useful for targeting certain mineral phases that are highly Raman active even at low concentrations, including S^0 and organic carbon. In this work, Raman microspectroscopy analyses revealed S^0 and organic carbon in nearly all of the sample materials, even though they were not detected with XRD (Table 1; **Supplementary Sections S2.2.1, S2.2.2**).

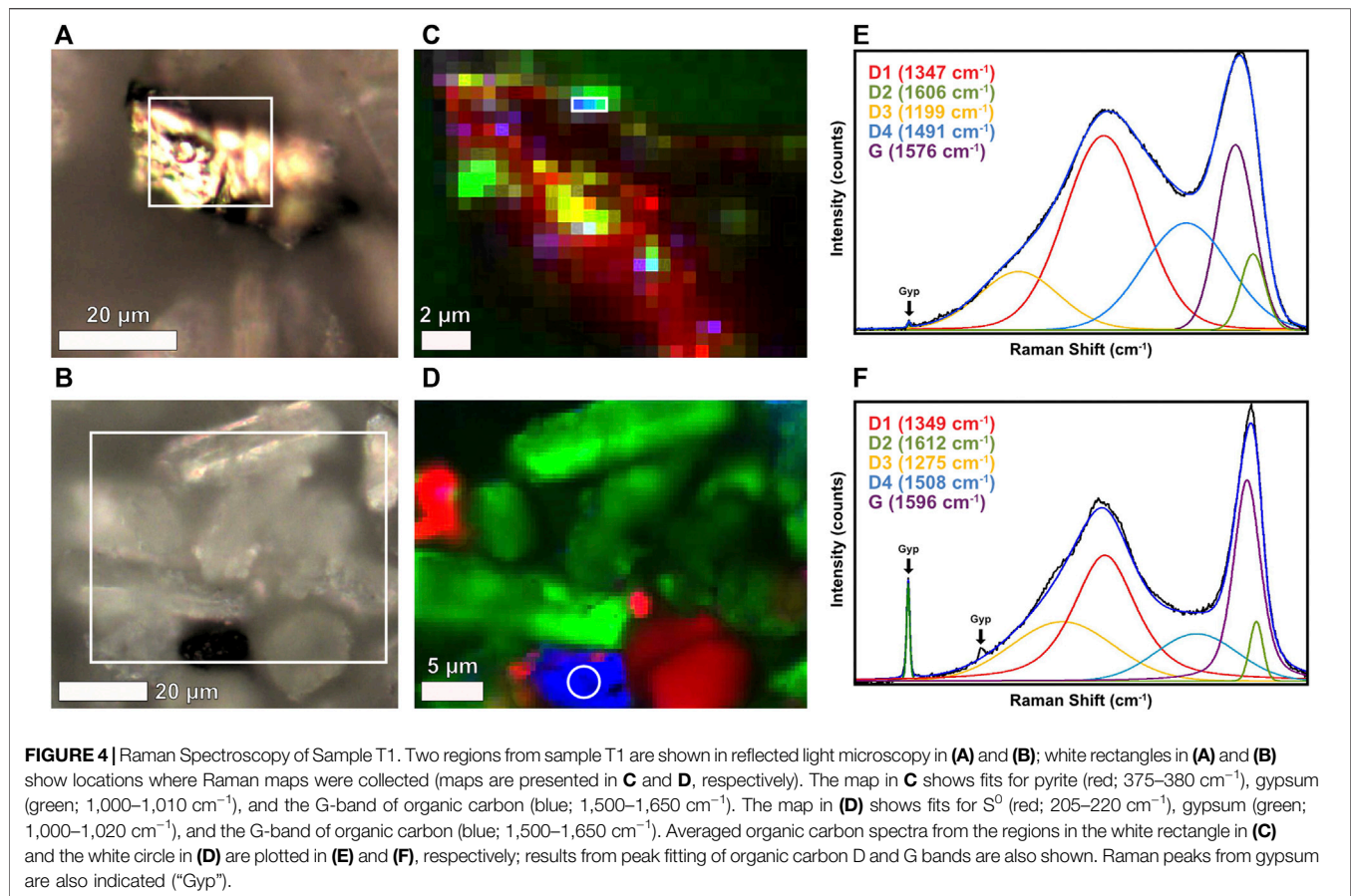
Raman microspectroscopy of sample T1 from site SF showed primarily tabular crystals of gypsum, with large pyrite grains (tens to hundreds of microns in width) and smaller spots containing elemental sulfur (S^0 ; Figure 4). Organic carbon is also detected in association with the pyrite and S^0 in this sample (see Figure 4; **Supplementary Figures S7–S8**). Sample T2, meanwhile, consists primarily of gypsum heavily stained in red/orange from the

occurrence of iron (oxyhydr)oxides, including goethite (**Supplementary Figure S9**).

The sidewall samples from site SF (S1, S2, and S3) show primarily tabular gypsum crystals. Sample S1 had an abundance of gypsum grains with associated sulfur and pyrite (Figure 5A). Sample S2, while similar, also had many regions containing red/orange stained gypsum grains with goethite and pyrite (Figure 5B). The pyrite grains in S1 and S2 also revealed associations with globules of elemental sulfur and organic carbon (Figure 5C; **Supplementary Figure S10**). Sample S3 appears to be composed primarily of gypsum and elemental sulfur with abundant organic carbon. A Raman spectral map for sample S3 also shows that organic carbon is associated with globular sulfur in this sample, while pyrite has not been detected in sample S3 (**Supplementary Figures S11, S12**).

The core samples from site SF show similar mineral morphologies and compositions to the sidewall samples, with an abundance of gypsum, pyrite, elemental sulfur, and organic carbon (Figure 6; **Supplementary Section S2.2.2.3**). Sample C1 contains large sulfide and gypsum grains (tens to hundreds of microns in width) with micron-sized spots bearing S^0 and quartz (Figures 6A,B). Sample C2 also contains large grains of pyrite and gypsum. One region from sample C2 contains tabular gypsum grains with spots of S^0 , pyrite, and organic carbon (Figure 6D). This region also appears to have the red/orange staining indicative of iron (oxyhydr)oxides, though these phases are not observed in the Raman map for this region (Figures 6C,D). Other regions of this sample show tabular gypsum grains encrusted in iron (oxyhydr)oxides, including hematite (Fe_2O_3). Sample C3 (**Supplementary Figures S16–S19**) revealed pyrite and gypsum together with iron (oxyhydr)oxide, while a large grain of pyrite (~50 microns by 80 microns) revealed associated gypsum, and hematite. This pyrite grain also had associated organic carbon, which is compared to organic carbon from a dark spot in/on a gypsum crystal in the same sample. C3 also had a region (~6 microns by 8 microns) that is rich in S^0 . Furthermore, a Raman map of one large pyrite grain revealed the presence of micron-sized spots bearing mackinawite and as-of-yet unidentified peak splitting of the pyrite spectrum. Sample C4 contains primarily pyrite, S^0 , gypsum, and organic carbon. There are S^0 - and OC-rich regions of the sample that are up to 10 μm in width (data not shown).

Reflected light microscopy and Raman microspectroscopy reveal that the NF samples are very similar to the materials from the trench-sampled feature (Figure 7; Table 1). All NF samples are primarily composed of tabular grains of gypsum with goethite, jarosite, and pyrite found in many places (Figure 7). In many ways, the NF samples are indistinguishable from those of the other feature, except that jarosite is abundant in the NF samples and was not detected in the other samples in these analyses (although jarosite was previously identified in SF surface materials through XRD by Grasby et al., 2012). Organic carbon is detected throughout the NF material, including in darker, isolated spots as were detected in the trench samples as well as one ~200 μm^2 region of organic carbon associated with two globules of S^0 (Figure 7; **Supplementary Figure S23**).



Raman microspectroscopy revealed regions apparently rich in organic carbon in all of the samples (Table 1; Supplementary Section S2.2.2.4). Organic carbon compounds are Raman active and can be detected through the presence of the D- and G-bands (“disordered” and “graphitic” bands, located at $\sim 1,350$ and $1,550\text{--}1,600\text{ cm}^{-1}$, respectively; sometimes a series of D-bands can be discerned around 1,150, 1,350, 1,500, and $1,620\text{ cm}^{-1}$ depending on the carbon compounds and the quality of the spectra; Ferrari and Robertson, 2000; Beyssac et al., 2002; Beyssac et al., 2003; Sadezky et al., 2005). These bands derive from the level of disorder among aromatic sp^2 -bonded carbon atoms. For instance, stretching vibrations in well-ordered aromatic carbon in the graphite arrangement will produce the G-band, while disorder in the structure of the organic compounds from in-plane defects, heteroatoms, and tetrahedral carbon interactions outside of the plane give rise to the D-bands (Beyssac et al., 2002; Beyssac et al., 2003; Broly et al., 2016). Most of the organic carbon detected in the alteration feature materials appears to be associated with pyrite, S^0 , and/or iron (oxyhydr)oxides within the samples; Figure 4 shows associations of organic carbon with both pyrite and S^0 in sample T1.

A comparison of the disordered (D) bands of organic material to the graphitic (G) bands can yield useful information regarding the alteration of the carbon (through thermal alteration and graphitization). For instance, the broad and overlapping D and G bands in organic carbon from these pyrite alteration features

(Supplementary Tables S1, S2) is generally indicative of disordered carbonaceous matter with low levels of carbonification and structural organization (e.g., Spötl et al., 1998; Ménez et al., 2012). This indicates lower-temperature formation of the organic carbon in these samples, but also makes it difficult to further constrain the thermal maturity of these materials.

A number of filamentous materials have also been observed within these materials (specifically in samples C2, C3, C4, and T2). Several spiral-shaped filaments were detected in sample C2 (Supplementary Figure S24). These filaments are $\sim 1\text{ }\mu\text{m}$ in width and tens of μm in length. Unfortunately, attempts to collect Raman spectra for these filaments were unsuccessful, as the filaments were so thin that the spectra returned showed only the glass slide in the background. A thicker filamentous structure ($\sim 10\text{ }\mu\text{m}$ width) was also detected in C2 and appeared to contain gypsum (see Supplementary Figure S24D). Thicker filaments ($\sim 5\text{--}10\text{ }\mu\text{m}$ widths) were also detected in samples C4 and T2 (Supplementary Figures S24E,F). The filament in sample C4 was highly fluorescent to the laser, but peaks for organic carbon were still discernible. Small spheroids of pyrite were attached to this filamentous structure. The filament in T2 was also fluorescent, but also revealed the presence of organic carbon. This filament appeared to be embedded in materials rich in goethite, quartz, and organic carbon (Supplementary Figure S9).

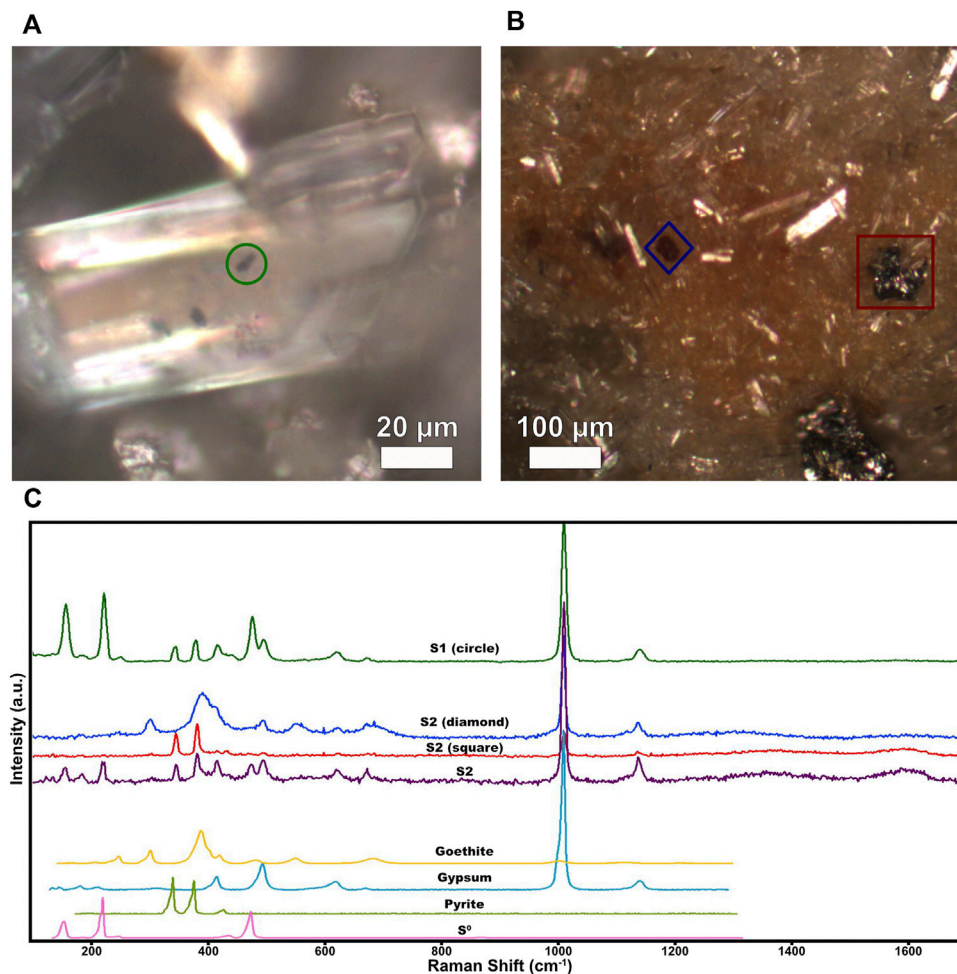


FIGURE 5 | Optical and Raman microspectroscopy of samples S1 and S2. A gypsum grain with associated dark grains of micron-sized pyrite from sample S1 is shown in **(A)**, while **(B)** shows a region of red/orange stained gypsum with iron oxide globules and larger pyrite grains within sample S2. Spectra presented in **(C)** show data for a pyrite grain from S1 (green circle in **A**) which bears pyrite as well as elemental sulfur (S^0) and also reveals gypsum. Spectra for a globule of goethite from S2 (blue diamond in **B**) and a pyrite grain from S2 with peaks for organic carbon (red box in **B**) are also shown. A spectrum is presented bearing peaks for S^0 and organic carbon, which comes from micron-sized spots on the pyrite grain in the red square in **(B)**. Reference spectra for pyrite, S^0 , gypsum, and goethite are also shown.

Electron Microscopy

SEM/EDS analyses were used for imaging and elemental analysis on samples C2, C3, and C4 from site SF. Outside of the expected tabular grains of gypsum, sample C2 revealed a large number of filamentous materials, which appear to be composed of, or coated in, aluminum-rich material (**Figure 8**). This material also contains oxygen, sulfur, and calcium. This sample also shows many gypsum crystals that are encrusted in materials that were determined to be aluminum and iron rich. Sample C3 materials included an aluminum-rich filament as well. Sample C4 contains abundant pyrite grains from 10 to 100 s of microns in size. These pyrite grains in many places appear to be geometrically etched, leaving grooves and polygonal holes (**Figure 8**).

Scanning Transmission X-Ray Microscopy

STXM allows for element-specific, nanoscale imaging of x-ray transmissive materials paired with nanoscale x-ray absorption

spectroscopy. STXM was used to map the distribution and characterize the speciation of carbon and sulfur in samples due to absorptions at the C K-edge and S L-edge. Samples that were analyzed using STXM include samples S2 and C4 from site SF (sidewall and core samples, respectively), as well as sample NF1. STXM data revealed the association of organic carbon with sulfate particles in the materials (**Figures 9, 10**). Sulfate, matching spectra for gypsum (Jalilehvand, 2006), was identified in micron-sized grains in all three samples; no other form of sulfur was detected in these materials using this sample preparation and analysis approach. Organic carbon was detected and mapped using STXM as well, with data from one region in sample NF1 (**Figures 9A–C**) showing defined carbon XANES peaks corresponding to aromatic and/or ketone functional groups as well as carboxylic groups (Brandes et al., 2004; Chan et al., 2010; Liu et al., 2013). In addition, organic carbon detected in two regions within sample C4 revealed the presence of two potentially

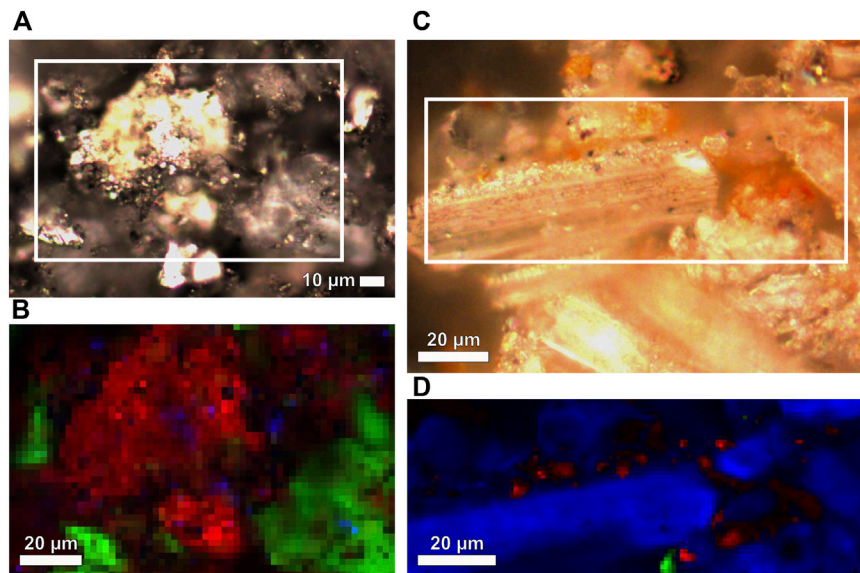


FIGURE 6 | Optical and Raman microspectroscopy of samples C1 and C2. Microscope images and Raman spectral maps are shown for samples C1 (**A,B**) and C2 (**C,D**). The white rectangles in microscope images show where maps were collected. The map for sample C1 shown in **B** is colorized to match fits for pyrite (red; 375–380 cm^{-1}), gypsum (green; 1,000–1,020 cm^{-1}), and the G-band of organic carbon (blue; 1,500–1,650 cm^{-1}). Quartz, S^0 , anhydrite, hematite, calcite, and silicon were also found in this map region (see text). The map for sample C2 shown in (**D**) is colorized to match fits for pyrite (red; 365–375 cm^{-1}), S^0 (green; 205–225 cm^{-1}), and gypsum (blue; 1,000–1,020 cm^{-1}). This map region also contains anhydrite and organic carbon.

different forms of carbon in this sample (**Figure 10**). One region (shown in the blue circle in **Figure 10A** and the blue spectra in **Figure 10D**) has a strong carbon XANES peak indicative of carboxyl functional groups ($1s \rightarrow \pi^*_{\text{C=O}}$). The associated dashed blue spectrum in **Figure 10D** (averaged over multiple small spots around the edges of a large gypsum grain in **Figure 10A**) may reveal further carbon XANES peaks, however these potential peaks may also be noise in data and are not interpreted further. Another region (shown in magenta in **Figure 10B** and the magenta spectra in **Figure 10D**) reveals the presence of unsaturated or aromatic carbon ($1s \rightarrow \pi^*_{\text{C=C}}$) as well as aliphatic and/or aromatic carbonyl groups, ketones, and/or phenols ($1s \rightarrow \sigma$; e.g., Brandes et al., 2004; Chan et al., 2010; Liu et al., 2013).

DISCUSSION

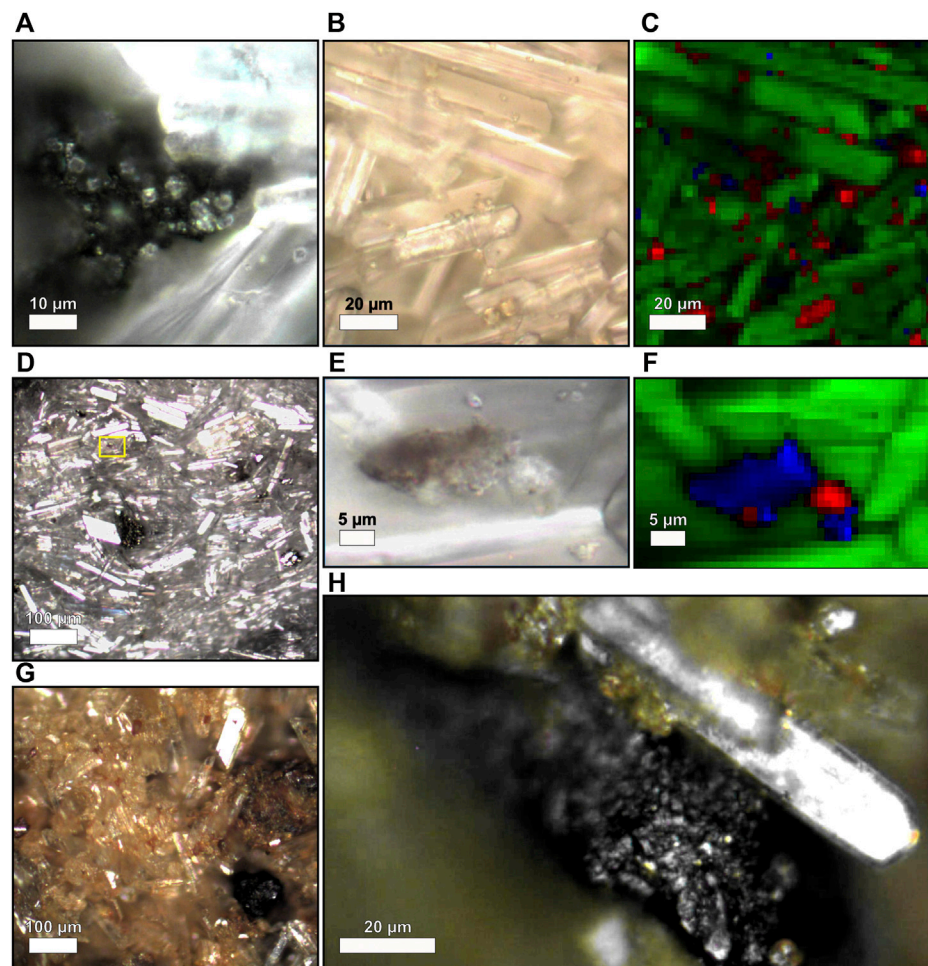
Source of the Pyrite and the Relationship to the Modern Sulfur Spring System

The conspicuous red-stained features at Borup Fiord Pass were previously described and discussed by Grasby et al. (2003), Grasby et al. (2012), and Scheidegger et al. (2012). These features have been implicated as remnants of springs similar to those that currently form sulfur-rich deposits and spring-derived ices (aufeis) at the toe of the glacier to the north of the features (Grasby et al., 2003, Grasby et al., 2012; Lau et al., 2017; Trivedi et al., 2020). The source of sulfur for this modern spring system has been proposed to be biological sulfate reduction (BSR) of subsurface anhydrite-bearing evaporite formations, as

evidenced through interpretations of local geology/hydrology and sulfur isotope systematics (Grasby et al., 2003; see **Figure 3**).

Grasby et al. (2012) proposed a model of sulfuric acid speleogenesis (SAS) for the formation of the red-stained mineral structures. In this model, spring conduits carrying sulfide-rich fluid from the subsurface formed beneath the local coalescence glacier when it was further south in extent. The oxidation of reduced sulfur species in such springs, forming sulfates as well as acidity, was then hypothesized to lead to the dissolution of local carbonates and replacement with sulfate minerals in the pipes carrying the spring fluids. After glacial retreat, permafrost advance would eventually cut off such spring conduits. The model of Grasby et al. (2012) then suggests that the mineral suite produced by spring activity would be “trapped” by being frozen in-place. These authors posited that the surface expression of the features, with their friable gypsum-rich materials, at the same topographic relief as the immediately surrounding native valley rock suggests that the features formed (at least partly) after the recession of ice from this region. This led for a constraint on the maximum age of the surface formation of the features to sometime within the last ~7,500 years (when glaciers in this region began to significantly retreat).

Our findings here require, at least in part, a reinterpretation of the nature of these iron- and sulfur-rich mineralized features. For instance, while Grasby et al. (2012) did not detect pyrite in the surface materials used in their study, we find abundant pyrite throughout the features, especially within the core material closest to the center of the trench in one feature (sample C1). Thus, it is important to recognize that processes occurred to



(Note: E is interior)

FIGURE 7 | Raman microspectroscopy of North Feature samples. Sample NF1 shows an abundance of gypsum with grains of pyrite, jarosite, and goethite throughout (A–C). The dark grain in (A) appears to be a grain of pyrite, which also reveals dispersed goethite, discrete granules of jarosite, anatase, and organic carbon, all set within gypsum. The microscope image in (B) and corresponding Raman spectral map in (C) show tabular grains of gypsum (green in C; $1,000\text{--}1,020\text{ cm}^{-1}$) with smaller grains of jarosite/hatrojarosite (red in C; $425\text{--}435\text{ cm}^{-1}$) and various organic carbon-rich spots (blue in C; $1,500\text{--}1,650\text{ cm}^{-1}$). Anatase and goethite were also detected in this map region. Pyrite grains are apparent within the gypsum matrix of NF2 (D). A yellow box in (D) highlights a region where a “goop” of organic material adhered to a gypsum crystal was detected. This material, shown in (E) and (F), revealed two globules of elemental sulfur (red in F; $205\text{--}225\text{ cm}^{-1}$) with a large clump of organic carbon (blue in F; $1,500\text{--}1,650\text{ cm}^{-1}$). The green in F signifies gypsum (fitting intensities from $1,000$ to $1,020\text{ cm}^{-1}$). Sample NF3 showed a greater abundance of red/orange staining from goethite (G). A low-resolution spectral map of the region in (G) revealed the presence of anatase, quartz, goethite, and gypsum in this region. One region showed a grain of gypsum along with abundant goethite and jarosite as well as organic carbon and anatase in sample NF3 (H).

induce pyrite emplacement in the near-surface. In addition, oxidative weathering of the pyrite in the features likely released acidity, playing a role in forming the current suite of oxidized iron and sulfur minerals (and leading us to term these as “mineral alteration features”). The alteration of the pyrite into more oxidized forms of Fe and S minerals, as we’ve detailed here, also appears to have developed a redox gradient within these features, from more reduced conditions near the central regions to more oxidized conditions in the outer regions of the features.

The extensive red staining of the region, and smaller pyrite veining in nearby carbonate rocks, suggests that pyrite emplacement in the region was more extensive than just within the features alone. Three potential mechanisms that

may reasonably have led to the emplacement of the pyrite in this region include: 1) magmatic sulfide ore derived directly from regional Mesozoic igneous intrusions; 2) pyrite derived from a geothermal system in conjunction with such igneous intrusions, with sulfur sourced from contact of a sill or dyke with a local, anhydrite-bearing evaporite unit; and 3) the low-temperature emplacement of authigenic pyrite from sulfide-rich fluids titrating ferrous iron from subsurface sources (where sulfide is derived from BSR of evaporite anhydrite).

Regional igneous intrusions are potential sources of thermal energy as well as iron and sulfur for the subsurface system that formed the pyrite in the structures under consideration (see Figure 1C). These intrusions are part of the High Arctic Large

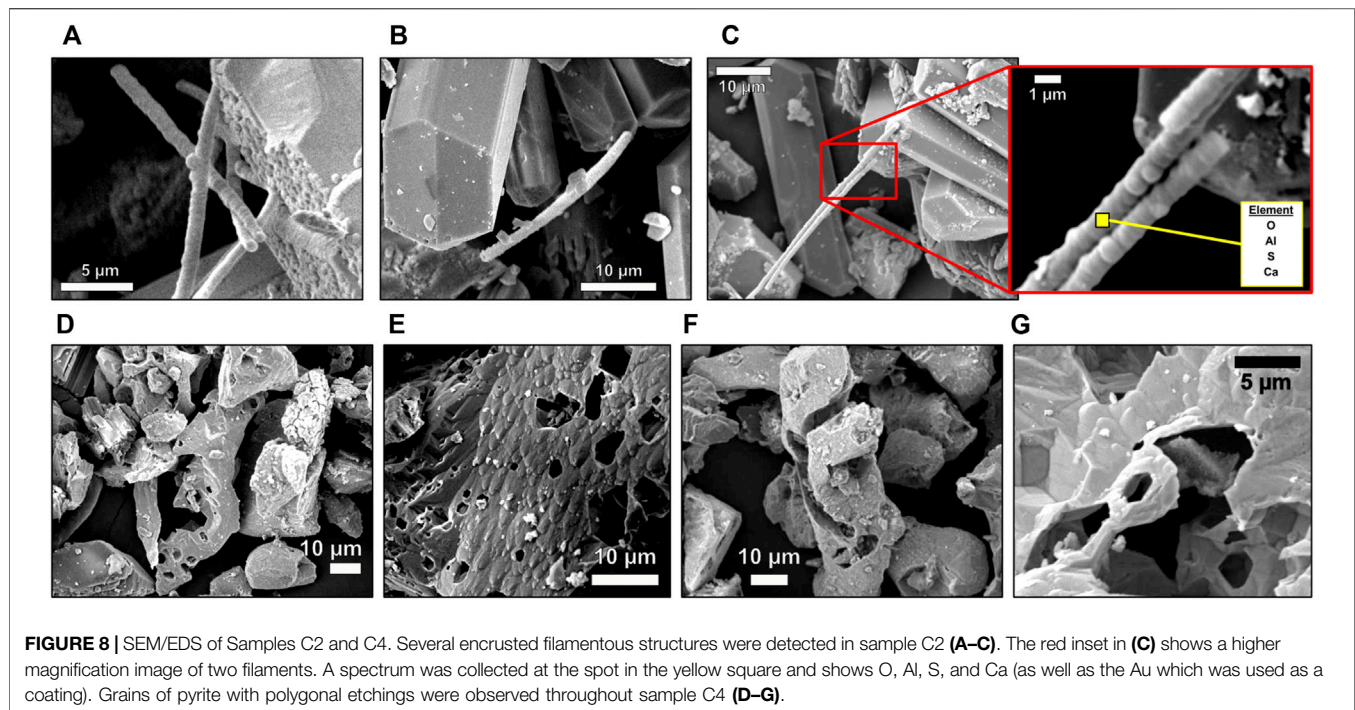


FIGURE 8 | SEM/EDS of Samples C2 and C4. Several encrusted filamentous structures were detected in sample C2 (A–C). The red inset in (C) shows a higher magnification image of two filaments. A spectrum was collected at the spot in the yellow square and shows O, Al, S, and Ca (as well as the Au which was used as a coating). Grains of pyrite with polygonal etchings were observed throughout sample C4 (D–G).

Igneous Province (HALIP), a predominantly intrusive, Cretaceous to Paleogene magmatic emplacement spanning much of the circum-Arctic region (e.g., Evenchick et al., 2015; Deegan et al., 2016; Saumur et al., 2016; Naber et al., 2020). Sills and dykes from these intrusions can be observed in the valley of Borup Fiord Pass (Grasby et al., 2003; Hill, 2014; **Supplementary Figure S3**). Although it is not known if an intrusion directly underlies the region of the pyrite mineralization for these features (and at what depth such an intrusion may be found), such magmatism may have been a source of thermal energy driving high-temperature emplacement of sulfide in veins around and within the local strike-slip fault in the valley (dashed line in **Figure 1C**).

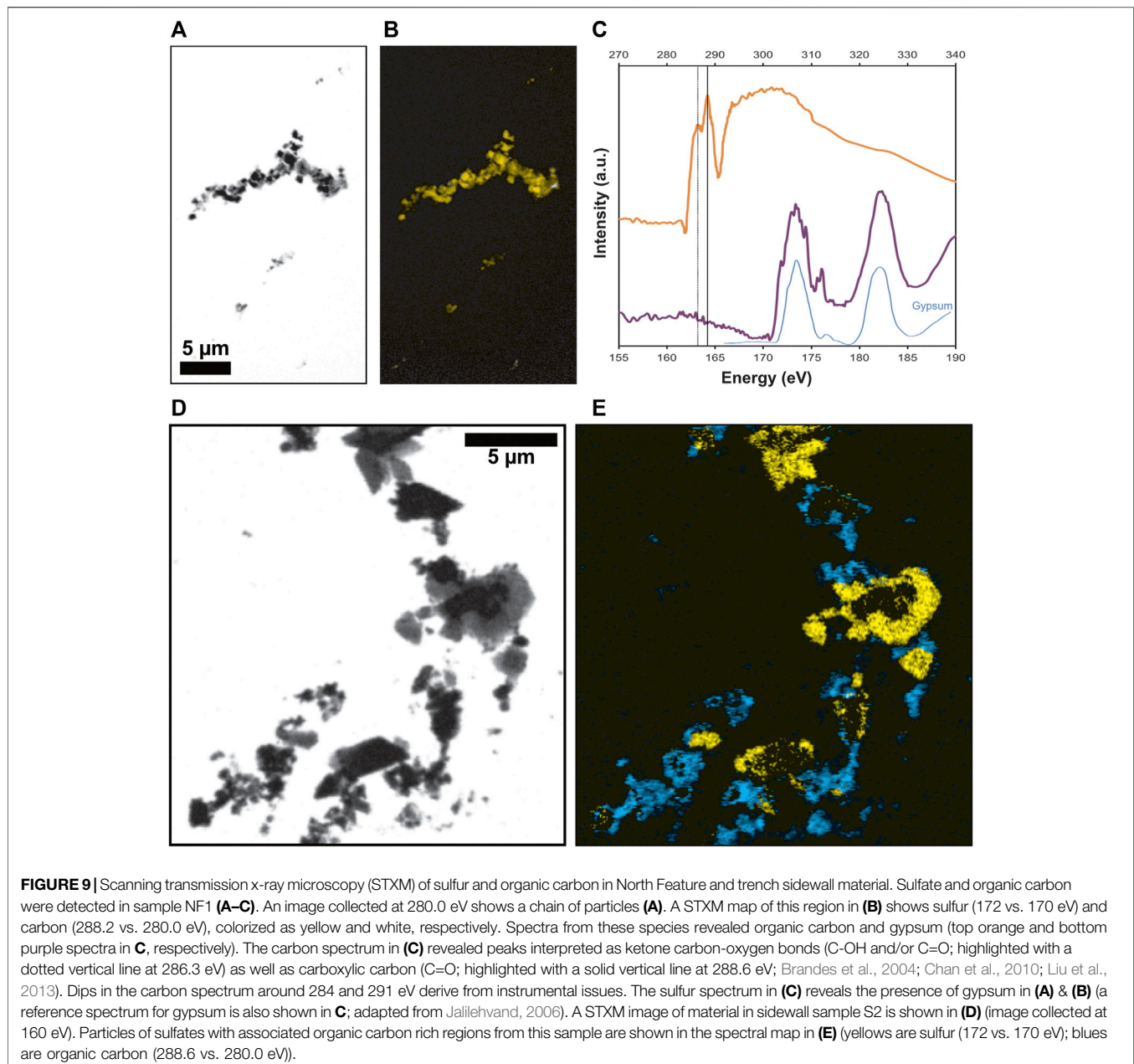
Magmatic intrusions can give rise to sulfide ore deposition through concentration of sulfur within the melt or through interaction with crustal sources of sulfur (Robertson et al., 2015; Barnes et al., 2017). In the region of the Sverdrup Basin, evaporite deposits are a likely source of crustal sulfur for such magmatic sulfide mineral formations.

Alternatively, geothermal processes could have formed pyrite within the red-stained features. Such geothermal activity would likely have been related to the intrusive magmatism discussed above. While high temperatures of metal sulfide formation in magmatic sulfides leads primarily to pyrrhotite and pentlandite, geo/hydro-thermal sulfide deposits most commonly consist of pyrite (Barnes et al., 2017; Fontboté et al., 2017). The sulfur for such hydrothermal deposits could again be derived from reduced magmatic sources or from the abundant crustal sulfate in local evaporite deposits.

There are two known anhydrite-rich evaporite units regionally, the Otto Fiord and Mount Bayley Formations. The Otto Fiord Formation is a Carboniferous evaporite formation

composed primarily of anhydrite (CaSO_4) and halite, with variable amounts of gypsum, limestone, and shale (Davies and Nassichuk, 1975; Grasby et al., 2003). This formation outcrops ~20 km to the north of Borup Fiord Pass (Davies and Nassichuk, 1975; Grasby et al., 2003). Stratigraphic constraints on the subsurface depth of the Otto Fiord Formation at Borup Fiord Pass range from hundreds of meters below the valley floor (Hill, 2014) to as much as 1.5–2 km in depth (Grasby et al., 2003; Gleeson et al., 2010). Meanwhile, the Mount Bayley Formation, which outcrops 19 km to the east of Borup Fiord Pass, is a Lower Permian evaporite unit of anhydrite, shale, and both fossiliferous and non-fossiliferous carbonates (Wallace et al., 1994). If the Mount Bayley Formation underlies Borup Fiord Pass, it may be within 200 m of the valley floor. However, it has been suggested that the formation appears to “pinch out” stratigraphically east of the valley (Gleeson et al., 2010; Gleeson et al., 2011).

If sulfate-rich rocks are the source of sulfur, the sulfate must first be reduced to sulfide to precipitate pyrite, through either thermochemical sulfate reduction (TSR) or BSR. TSR and BSR occur in much different thermal regimes. TSR often requires minimum temperatures from 100 to 140°C (although in some systems TSR requirements of 160–180°C have been observed; Machel, 2001). As described by Grasby et al. (2003), permafrost from an oil well 43 km to the south of Borup Fiord Pass has been measured at 540 m, suggesting potentially even deeper permafrost at Borup. Moreover, with the local geothermal gradient of 22°C km⁻¹ beneath the base of the glacier/permafrost (Grasby et al., 2012), TSR could only occur if sulfate-enriched fluids from the dissolution of the Otto Fiord or Mount Bayley Formations travel as deep as 5–6 km into the subsurface. Lithostatic pressure at this depth precludes fluid flow, and thus TSR is not likely the source of sulfide in modern springs.



However, TSR could still have occurred previously if circulating fluids were heated during Cretaceous magmatism.

Biological sulfate reduction is the likely pathway for reduced sulfur within the modern sulfur springs at Borup Fiord Pass since there is currently no known source of high temperatures for TSR within the modern system (Grasby et al., 2003). Subsurface BSR may also have been active in the past as well, giving rise to the sulfide (pyrite) now extensively mineralized in the shallow subsurface. One way to distinguish between TSR and BSR is evaluation of the isotope systematics of sulfate and sulfide. TSR does not impart a significant fractionation of sulfur isotopes (Machel, 2001). Thus, in the case of TSR the sulfur isotope composition of the pyrite mineralization would closely match

the $\delta^{34}\text{S}$ of the known evaporite units underlying Borup Fiord Pass. In contrast, in BSR dissimilatory sulfate reducing organisms have a selective preference for ^{32}S over ^{34}S , which can give rise to diagnostic sulfur isotope fractionations (e.g., Thode, 1991). Thus, if BSR is occurring in subsurface fluids enriched in sulfate from the dissolution of Otto Fiord or Mount Bayley Formations, sulfide should be depleted in $\delta^{34}\text{S}$ relative to the source anhydrite. As shown in **Figure 3**, the isotopic offset between the local geological sulfates and the pyrite in the features (6.5‰ in C1, 8.5‰ in C2, and 11.7‰ in NF1) are sufficiently large that BSR can reasonably be invoked.

An interpretation of sulfur for the features being sourced through BSR of local anhydrite units still necessitates a

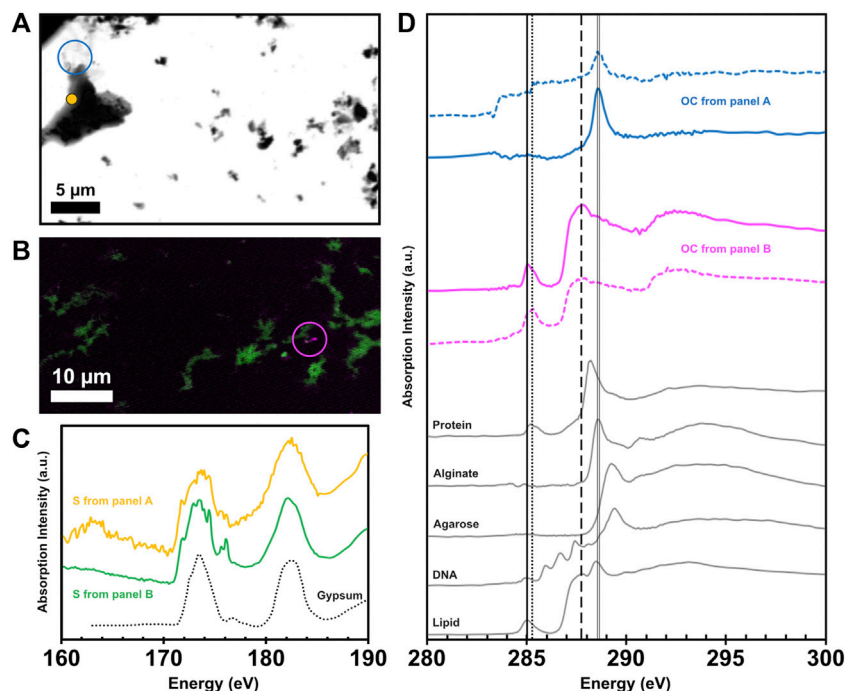


FIGURE 10 | Scanning transmission x-ray microscopy (STXM) and x-ray absorption near edge structure (XANES) spectroscopy of sulfur and organic carbon in trench core material. Two regions of core sample C4 are presented (**A, B**), showing the collocation of sulfur and organic carbon (identified with sulfur and carbon XANES spectra in **C** and **D**, respectively). A STXM image collected at 320.0 eV (**A**) shows particles identified as gypsum (see representative yellow spectrum in **C**, collected from the location in **A** of the yellow circle). The blue circle in (**A**) shows the location of collection of the solid blue carbon spectrum at the top of (**D**) (the dashed blue spectrum represents organic carbon from smaller spots distributed around the largest gypsum-rich grain). A STXM map of sulfur and carbon is presented in (**B**), where green represents the difference in sulfur absorptions between 170 and 172 eV, and magenta represents the difference in carbon absorptions between 280 and 288.2 eV. The green spectrum in (**C**) represents gypsum detected throughout the green regions in (**B**). The magenta circle in (**B**) highlights the location of collection of the solid magenta carbon XANES spectrum shown in the middle region of (**D**) (the dashed magenta spectrum represents organic carbon from smaller spots distributed throughout the material in **B**). A reference spectrum for gypsum is shown in **C** (data adapted from Jallilehvand, 2006). Reference spectra for multiple organic carbon compounds are also shown in (**D**). These reference data are reported by Chan et al. (2010) and are as follows: a protein (bovine serum albumin; BSA), alginate (an acidic polysaccharide), agarose (a neutral polysaccharide), a sample of DNA, and a lipid (1,2-dipalmitoyl-sn-glycero-3-phosphoethanolamine). Vertical lines, included to highlight the carbon functional groups in the sample spectra, represent the following carbon functional groups: unsaturated or aromatic carbon ($1s \rightarrow \pi^* C=C$; solid line at 285.2 eV and dotted line at 285.4 eV); aliphatic carbon, aromatic carbonyl, ketones, and/or phenols ($1s \rightarrow \sigma$; dashed line at 287.6 eV); and carboxyl ($1s \rightarrow \pi^* C=O$; double lines; 288.6 eV; see references in the text).

geological source of iron and a mechanism for iron titration forming pyrite at low-temperature. The local Cretaceous igneous intrusions and the Permian-aged Esayoo Bay lavas at Borup Fiord Pass (**Figure 1C**) may provide a source of ferrous iron for the formation of pyrite in the alteration features. However, it is beyond the scope of the data collected for this study to specify the exact source of the iron within the features.

Weathering of Pyrite: Gossans in Permafrost

Given the extent of red staining from iron (oxyhydr)oxides in the alteration features at Borup Fiord Pass and the red staining of rocks and pyrite veining in the surrounding region, we infer that the pyrite mineralization emplaced beneath the surface of this region has been subsequently weathered. The oxidation of pyrite by oxygen and ferric iron (often driven and accelerated by biology) produces ferric iron (oxyhydr)oxides, sulfates, and acidity. The mineralogical suite we detect in the alteration

feature materials, with an abundance of iron (oxyhydr)oxides in the presence of pyrite and gypsum (**Table 1**), are reminiscent of acid mine/rock drainage systems (e.g., Edwards et al., 1999; Fernández-Remolar et al., 2005; Taylor and Konhauser, 2011). Our detections of minerals common in such systems of pyrite oxidation (e.g. hematite, goethite, jarosite, sulfates) suggest to us that the alteration features represent emplacements of pyrite that have since been altered to form their current oxidized iron and sulfur mineralogical structure. Also, lowered pH does not increase silica solubility, explaining the abundances of quartz in gossans (Taylor and Eggleton, 2001), where silicate minerals are often leached in the acidic system leaving behind quartz. This may explain the abundance of quartz detected in these Arctic features as well.

The nearly identical $\delta^{34}\text{S}$ values for sulfides and sulfates in the alteration features suggests that the sulfates (primarily gypsum) formed from the oxidation of the sulfide, a process that is not commonly thought to impart a significant fractionation of sulfur isotopes (e.g., Zerkle et al., 2009). The production of sulfates from

the oxidation of pyrite also releases acidity. The discovery through SEM/EDS of filamentous materials that appear enriched in aluminum (**Figure 8**) reveals the importance of acidity in alteration feature formation. The presence of aluminum-rich materials suggests that aluminum had at one time been mobilized in this system, and aluminum is only stable in solution at significant concentrations when pH is very low or, to a lesser degree, very high (e.g., Hem, 1985).

Gossan sites on Victoria Island (Northwest Territories, Canada) also present materials indicative of pyrite alteration including gypsum, goethite, jarosite, and hematite, all in a permafrost-rich environment (Percival and Williamson, 2016). In particular, the site called Gossan Hill is topographically high compared to the surrounding region, possibly due to the presence of pyritic sand and erosion resistant iron oxides in the soil (Peterson et al., 2014), and is similar to the topographically high region at Borup Fiord Pass that hosts the alteration features in this study (**Figure 1; Supplementary Figures S1, S3**). Gossan Hill also bears concentric gossan features, with interior regions dominated by gypsum and quartz, a yellow-stained border with gypsum, quartz, and jarosite, and then a brown colored rim with quartz and ferric (oxy)hydroxides. Below the surface, the central regions also contain quartz and pyrite along with S^0 . Also in common with the alteration feature region at Borup Fiord Pass, Gossan Hill is underlain by carbonate with inter-bedding of sulfate evaporites (Peterson et al., 2014).

Due to the presence of permafrost at Borup Fiord Pass, it is likely that little oxidation of the pyrite can occur at depth in this gossanous system. In terrestrial gossans at lower latitudes, iron oxides are often leached downward through the gossan from infiltration by meteoric waters (e.g., Taylor and Eggleton, 2001). However, a pyrite vein in permafrost will not see infiltration of fluids and rather will likely leach horizontally along the active zone. We infer this as the reason for the white central regions rich in gypsum in the two largest alteration features, as well as for the anatase and quartz that were detected within these materials.

The question arises as to what fluid source allows for pyrite alteration in these features. Even though Borup Fiord Pass receives a minor amount of precipitation annually, the melt and refreezing of snow and ice likely imparts a significant volume of water into the alteration features and surrounding region. For instance, during the process of digging the trench and drilling cores for this study, we encountered several cavities within the features. Deployment of a camera into some of these cavities revealed significant amounts of water ice around the rims of the cavities. Furthermore, summertime temperatures at the site of the alteration features can be quite mild, allowing for the melt of glacial ice and snow and providing a source of fluid for pyrite alteration. This was observed by glacial melt streams, lakes, and water-logged sediments throughout the region of the alteration features.

The Role of Biology in the Formation of the Pyrite Alteration Features: Development of a Potentially Habitable System

There are two potential roles for biology in the cycling of sulfur and the formation of the mineral assemblages in the alteration

feature region at Borup Fiord Pass: 1) reduction of sulfate to sulfide in the subsurface through BSR and 2) the oxidative alteration of the pyrite at the surface to form the gossanous suite of minerals. Both processes harness the dominant forms of chemical energy available and are excellent indicators of a habitable and/or inhabited system. BSR is dependent upon there being a source of reductants (e.g., organic matter or H_2) present to drive sulfide production; the later pyrite oxidation, forming the alteration features and their suite of minerals, involves the oxidation of Fe(II) to ferric phases and the oxidation of reduced sulfur to elemental sulfur and sulfates.

Pyrite is abundant in the materials we explored in this work. We have demonstrated the presence of pyrite in surface and near-surface samples within the active zone (T1, S1-2, and NF1-3), as well as within all four of the core samples from the permafrost of SF. In addition, when extracting grains for submission for sulfur isotopes, it was observed that opaque, metallic grains $>425 \mu m$ in diameter made up $\sim 45\%$ of sample C1 (these grains were later confirmed by EA-IRMS to bear 54% sulfur, roughly the expected concentration of sulfur in pyrite). Our data and these findings suggest that pyrite may be abundant in the central regions of these features, especially at depth. The alteration features may thus be windows into previous subsurface processes, including BSR and subsequent titration of geologically available iron.

Previous research from Grasby et al. (2003), Gleeson et al. (2011), Gleeson et al. (2012), Grasby et al. (2012), Lau et al. (2017), and Trivedi et al. (2020) has explored both the modern spring system as well as the alteration feature system at Borup Fiord Pass as habitable analogs for astrobiological research. One key factor in these studies has been the role of life in the cycling of sulfur through reduced and oxidized species, such as from BSR in the subsurface, where the reduction of local geological sulfates by microbial metabolisms has led to sulfide rich springs emerging in the modern day and may have similarly been responsible as the source of sulfide for the pyrite in the alteration features explored in this study. While pyrite formed through BSR in sedimentary deposits may be the largest source of pyrite at Earth's surface (Bottrell et al., 2006; Rickard, 2012; Rickard et al., 2017), the production of pyrite emplacements in the near surface from fluids enriched in sulfide due to BSR are an intriguing target for understanding the habitability of the subsurface in such systems. However, these features also provide a unique target in understanding the potential role of biology in the alteration of the pyrite to oxidized Fe and S minerals, as well as for such alteration to provide a habitable system for living processes.

The acidic weathering of sulfide minerals driving alteration to sulfates and ferric (oxyhydr)oxides provides energy for life in various environments on Earth, ranging from acid mine/rock drainage systems (Amils, 2016; Edwards et al., 2000a) to terrestrial gossans and other pyritiferous weathering systems (Percival and Williamson, 2016; Grasby et al., 2021). Such systems produce not only diagnostic mineral assemblages but also chemical and redox gradients that make them potentially habitable systems (e.g., Zolotov and Shock, 2003; Grasby et al., 2021).

Our work here presents these features at Borup Fiord Pass as potentially habitable pyrite alteration features. The features we

have characterized are primarily composed of gypsum with the inclusion of Fe-oxides, driving the surface colorations as previously noted by Grasby et al. (2012). However, using XRD and Raman microspectroscopy, we notably also detected pyrite, S^0 , and organic carbon in nearly all of the samples from the trench at site SF (Table 1). Also, while the red coloration of the outer region of this feature is visually apparent and goethite is detected in sample T2 through XRD, iron (oxyhydr)oxides (primarily goethite and hematite) were also detected through Raman microspectroscopy within the interior of the trench and in the permafrost (samples S2 and C1-C3). Although jarosite was detected at low concentration in the outer region of the surface at site SF by Grasby et al. (2012), we did not detect jarosite in any of the samples from the trench, even though jarosite was detected in all three samples from the North Feature. Also, while the surface transect of samples from Grasby et al. (2012) did not contain detectable pyrite, quartz, or anatase, these minerals are detected in several samples throughout the trench of SF as well in samples from site NF (Table 1).

The feature at site NF has not been previously reported. This feature is on the edge of the topographically high region and exhibits a similar mineralogy to the other red-stained structures (Table 1; Supplementary Figures S1–S3). This feature does not bear the familiar gypsum-rich white core of the two larger mineral alteration features. Instead, site NF has developed red-staining from iron (oxyhydr)oxides mixed with pebbles and cobbles of carbonate rock. There are additional dissimilarities in the surface mineralogy. Along with pyrite and gypsum, site NF also contains abundant jarosite, detected through both XRD and Raman microspectroscopy (Table 1; Figure 7). Also, quartz and goethite were detected in each NF sample, while S^0 was only detected in NF2 (through Raman spectroscopy; observed to be scarce in sample material) and anatase was detected in NF1 and NF3.

The detections of anatase (TiO_2) and quartz (SiO_2) in these features is intriguing and may indicate that the features are derived from some level of geo/hydro-thermal activity. Titanium is usually considered an immobile reference element in alteration processes, although it is soluble at very low and high pH (Tilley and Higgleton, 2005). However, anatase is commonly found in hydrothermal and metamorphic systems (Banfield et al., 1993; Tilley and Higgleton, 2005). TiO_2 minerals (e.g., anatase, rutile, brookite) often occur as fine crystals in other minerals and can be difficult to study through XRD (Banfield et al., 1993), however the implementation of Raman microspectroscopy in our study allowed for the microscale identification of anatase in these samples.

It is currently unknown what fraction of the organic carbon inventory in these features may derive exogenously (e.g., from BSR or other organic carbon sources in the subsurface) and how much, if any, of the organic carbon may have formed *in situ* through biological processes involved in the alteration of the pyrite, thereby being a target for future biosignature analysis. Beyond potential subsurface sources, organic carbon may be present in the surface materials from the interactions of tundra plants and animals (muskox and Arctic hare were observed at the site in 2014) and soil microbial processes of

the valley. Also, pre-glacial soils may have imparted a significant fraction of organic matter regionally (for instance, glacial till at the toe of the glacier in 2014 had 2.5 wt.% TOC; unpublished data). In the alteration features, sample T2 had the highest TOC at 0.37%, but also is close to nearby tundra plants and soil. However, we cannot infer how much of that carbon may come from surface sources and how much is primary.

We hypothesize that much of the carbon either comes from subsurface sources or was formed *in situ*. Although we cannot preclude exogenous sources of organic carbon in the alteration features, Raman microspectroscopy reveals a close association of the organic carbon with pyrite, S^0 , and iron (oxyhydr)oxides in the materials (though conspicuous dark grains of OC either on or in grains of gypsum are also detected). The material from site NF (specifically sample NF2) also has an organic carbon-rich region of $\sim 200 \mu m^2$, identified through Raman microspectroscopy, where the organic carbon is associated with two globular regions of elemental sulfur (Figures 7D–F; Supplementary Figure S23). These elemental sulfur regions are 2 and 4 μm in diameter and, together with the organic carbon glom, are found in a region of tabular gypsum crystals and large grains of pyrite. These co-associations of organic carbon and S^0 in a region of pyrite and gypsum may indicate biological activity in the formation of the elemental sulfur regions. Perhaps even more intriguingly, organic carbon is found associated with sulfur minerals across a range of oxidation states, supporting the proposal that a redox gradient within the system may provide an impetus for living microorganisms to inhabit these features.

Our STXM data also show associations of organic carbon with sulfates in these materials (Figures 9, 10). For instance, a carbon spectrum derived from one region in sample NF1 showed the presence of carbon and oxygen bonds inferred to be aromatic and/or ketone functional groups as well as carboxylic groups (Brandes et al., 2004; Chan et al., 2010; Liu et al., 2013). While we do not have sufficient data to determine the specific organics that are present, our spectra do appear compatible with the presence of lipids or polysaccharides. However, our data do lack a signal from amide functional groups in proteins (which should show a peak at 288.2 eV); this may indicate a lack of microbial cell abundances within the materials.

Although we cannot here determine the source(s) of organic carbon that we've identified in the alteration feature materials and our STXM data may indicate a lack of microbial cells, some potential indicators for biological activity in the process(es) of pyrite alteration are demonstrated in this work. For instance, pyrite grains within the alteration features are geometrically etched (Figure 8), similar to etchings which have previously been identified in microbial leaching patterns in pyrite (e.g., Edwards et al., 2000b; Rojas-Chapana and Tributsch, 2004). Also, the abundance and variety of filamentous structure detected in the alteration feature materials (Figure 8) may indicate potential biological activity. For instance, the aluminum-rich filaments in the alteration features resemble similar structures that have been implicated as forming through microbial processes from a variety of low-temperature, subsurface sites globally (e.g., Hofmann and Farmer, 2000). If such filaments formed through biological

processes, they may then have later served as sites for precipitation of aluminum oxides from aluminum which had been mobilized in the low-pH system caused by the oxidation and alteration of the pyrite. However, recent work by Cosmidis et al. (2019) and Cosmidis and Templeton (2016) shows that systems rich in organic carbon and sulfide can abiotically form carbon and sulfur rich microstructures, reminiscent of filaments previously identified and implicated as forming from biological processes in the Borup Fiord Pass sulfur spring system (Gleeson et al., 2012). The filaments identified in the alteration feature materials share some sizes and morphologies with these abiotic filaments presented by Cosmidis and Templeton (2016), though this does not preclude biological activity in formation of filamentous materials within the alteration features. Further work will be necessary to better understand the composition and nature of these microstructures.

The Pyrite Alteration Features as Analogs for Potential Mineralized Paleohydrological Features on Mars

Pyrite alteration features and gossans such as the features we have explored at Borup Fiord pass may be ideal targets in the search for past or present life as well as potentially habitable systems on Mars (should they exist there). High concentrations of iron and sulfur in the Martian regolith were first detected by the Viking XRF instrument (Toulmin et al., 1977) and have since been confirmed with APXS instruments onboard multiple Mars rovers (e.g., Gellert and Clark, 2015). The potential for the emplacement of iron sulfide ores in the Martian subsurface and subsequent oxidative leaching via gossanous systems has been considered by Burns (1987) and Burns and Fisher (1990a), Burns and Fisher (1990b). They have proposed that komatiitic basalts on Mars likely host sulfide deposits rich in pyrrhotite and pentlandite (similar to known Earth-based analogs). Also, sulfides formed from sulfate reduction through thermochemical and potentially biological processes may also exist on Mars.

Although rare, sulfide minerals have been identified from several locations on Mars through surface rover instrumentation, including the potential detection of pyrite/marcasite in sample Fuzzy Smith at Home Plate in the Columbia Hills from Spirit (Squyres et al., 2007; Morris et al., 2008) as well as the detection of pyrrhotite in samples John Klein and Cumberland in Gale crater from Curiosity and the detection of pyrite, though at/near detection limits, in sample John Klein (Vaniman et al., 2014; Hurowitz et al., 2017; Rampe et al., 2017). More recently, reduced sulfur has been inferred from evolved gas analyses of samples at Vera Rubin Ridge, suggesting that sulfur redox chemistry has played an important role in the geological history of the region (Wong et al., 2020). Sulfides have also been identified within Martian meteorites (e.g., King and McLennan, 2010; Tarnas et al., 2021; and references therein), however the abundance and distribution of sulfides on Mars is currently not well constrained and the lack of detections suggests that sulfides are not common in easily accessed surface materials.

Oxidative weathering of Martian sulfide ores (should they exist) and other pyritiferous materials in near-surface

environments would follow pathways similar to those for known gossanous systems on Earth, and the strong redox gradients established may have provided habitable systems for life (e.g., Percival and Williamson, 2016; Grasby et al., 2021). There are abundant oxidized iron and sulfur minerals identified through remote sensing and from surface observations on Mars (e.g., Ehlmann and Edwards, 2014), though it is unknown yet if any such features may indicate pyrite alteration, regionally or locally. The presence of sulfates associated with hematite spherules at Meridiani Planum, as detected by the Opportunity rover, has been interpreted as having formed through the emplacement of sulfide ore followed by later oxidative leaching, creating the jarosite-goethite-gypsum assemblage observed (Zolotov and Shock, 2005; though other interpretations also exist, c.f.; Squyres et al., 2004; McCollom and Hynek, 2005). The emplacement of parent pyrite in such a system was hypothesized by Zolotov and Shock (2005) to have formed through hydrothermal input of sulfide, however it is also possible that low-temperature pyrite emplacements exist on Mars. Furthermore, recent work by Peretyazhko et al. (2021) suggests that the presence of akageneite in various localities in Gale crater implies the oxidative alteration or oxidation-hydrolysis of iron sulfide (namely pyrrhotite) in an acidic system.

It appears likely that there have been and may still be emplacements of iron sulfides and pyritiferous materials on Mars. However, even in the absence of abundant surface expressions of iron sulfide minerals, there are a variety of oxidized iron and sulfur materials that resemble, at least in part, the mineral assemblages we see in these alteration features from the Arctic. Beyond abundant iron and sulfur minerals on Mars' surface, veins of calcium sulfates (gypsum and/or bassanite) have been detected by both the Opportunity rover in Endeavour Crater (Squyres et al., 2012) and by the Curiosity rover within Gale Crater (Nachon et al., 2014; Rapin et al., 2016). Also, light-toned materials that were excavated by the Spirit rover in a region with abundant sulfates (Wang et al., 2008) revealed material that resembles the surface expressions of our sample SF as shown in **Figures 2B,C**. Our current and future explorations of Mars will allow for further interrogation of regions enriched in sulfates and iron mineralogies. Should they be similar to what we report for the alteration features from Borup Fiord Pass, then such mineral suites on Mars may be diagnostic of potential systems where sulfides were emplaced and subsequently weathered, perhaps through focused fluid flow in a system allowing for pyrite emplacement (as we hypothesize to potentially have occurred at Borup Fiord Pass) or through other processes such as igneous emplacement (Burns and Fisher, 1990a). Such regions may be primary targets for drilling and sample collection to explore for sulfides in the subsurface as well as potential indications of past or present biological activity.

Although the preservation potential for organic materials in acidic iron-rich systems on Mars may be limited (e.g., Sumner, 2004), the prevalence of such systems on Mars and the potential for their forming a habitable refuge for life make them a key target

for Mars exploration. Our work on the pyrite alteration features at Borup Fiord Pass presents organic carbon as well as etching of pyrite grains and the formation of filamentous structures as potential targets for further exploration of the potential role of biology in the system at Borup Fiord Pass, and such features could also be initial indicators for further work on systems identified on Mars.

Unfortunately, during the course of our field work, the materials that were collected from the alteration features were not collected in a manner that would allow for a well-resolved extraction and characterization of the organic carbon and/or potential lipid biosignatures through methods such as gas chromatography mass spectrometry (GCMS). However, the initial indications through Raman and STXM along with detections of mineral etchings and microstructures in such alteration features relate directly to current and future research on the Martian surface, specifically being carried out by the Perseverance rover at Jezero Crater and with the upcoming ExoMars rover Rosalind Franklin at Oxia Planum.

Perseverance is the first mission to use Raman spectromicroscopy on the Martian surface (Farley et al., 2020) and is capable of detecting and analyzing organic carbon (Beagle et al., 2014; Bhartia et al., 2021). Should such detections be made, it is highly likely that a sample will be collected and cached as part of the sample return architecture of which Perseverance is taking part (Farley et al., 2020). Such returned samples will certainly be scrutinized with a variety of methods and may include high resolution synchrotron based methods such as STXM. These returned samples will also allow for high resolution microscopy paired with other methods to explore the potential for organic and mineralized filaments and other microstructures such as we observe in these Arctic alteration features. While current observations do not suggest pyrite alteration features may exist within Jezero Crater, our samples from the pyrite alteration features at Borup Fiord Pass may serve as a strong rationale for seeking organic carbon in such alteration mineral suites, to detect potential biosignatures within future samples returned from Mars.

The Rosalind Franklin rover will also feature a Raman spectrometer along with its suite of instrumentation; however, this mission will also have a drill potentially capable of reaching depths up to 2 m (Vago et al., 2017). Drilling to such depths will allow for the collection of organic materials that have been less effected by exposure to cosmic radiation and surface oxidants. Intriguingly, this may also allow for exploration of potential iron sulfide minerals in the subsurface that lead to alteration mineral assemblages in surface materials. The potential for life detection along with exploring subsurface geochemistry and mineralogy with the Rosalind Franklin rover also highlights the importance of further exploration of our Arctic alteration features.

Future work on the alteration features at Borup Fiord Pass should include sample collection and analyses that allow for rigorous characterization of the organic carbon present and to potentially target lipids that may have preserved evidence of the activity of iron- and/or sulfur-oxidizing microbes in the alteration features. Furthermore, a future study may seek to deploy a coring drill capable of exploring a great depth into the permafrost of the

features in order to better explore the mineralogical structure of the features, especially as we have here argued that pyrite appears to be more abundant at depth.

CONCLUSION

Our findings show that conspicuous mineral alteration features at Borup Fiord Pass combine iron and sulfur minerals in a suite of oxidation states (from most reduced Fe and S near the cores of the structures to more oxidized forms at the rims). We infer that pyrite is more abundant in the subsurface and that oxidative weathering of the pyrite is forming this unique mineral assemblage, and furthermore that these and similar features may preserve unique ecological niches.

In this work, we have asked whether or not sulfate-rich pyrite alteration features may be good astrobiological targets that preserve evidence of habitable environments on Mars as well as at Borup Fiord Pass. We show that pyrite is abundant in the alteration features from Borup Fiord Pass, especially within cores taken from below the active zone. Isotopic data suggest that the sulfide in the pyrite could have come from BSR of subsurface anhydrite, and thus these mineralized features may be derived from prior biological activity. However, we also present two other potential mechanisms for the emplacement of the pyrite in the system, specifically magmatic pyrite and hydrothermal pyrite related to the intrusion of Mesozoic dykes and sills regionally; all three processes should be further explored to determine the source of pyrite in these features.

Our integrated mineralogical analyses reveal pyrite, S^0 , and gypsum co-localized within these features, preserving strong chemical disequilibria represented by multiple oxidation states of sulfur. Also, we find a mineralogical suite including iron (oxyhydr)oxides co-associated with the sulfates that is indicative of pyrite alteration. Abundant red-staining and pyrite veining in materials within the alteration feature region also suggest large-scale pyrite alteration. Organic carbon is abundant in these materials, as are geometrically etched pyrite grains and aluminum-encrusted filamentous materials, raising the possibility that these features preserve physical and chemical signals of subsurface and surface biological activity. Further research on these features should include detailed work on potential biological processes, including DNA extraction and sequencing and detailed characterization of the organic materials present.

The emplacement of pyrite and subsequent leaching to form an alteration mineralogy (potentially through biological action) presents a high-quality target for our future geological and astrobiological explorations of Earth and Mars. Gossanous systems may preserve signatures of biological processes that occur during the oxidative alteration of emplaced pyrite, and such systems may present topographically high features for initial indication of their presence, warranting further exploration. Discovery of a pyrite rich mineral alteration feature and/or system on Mars will require further data and interpretations of the importance of sites like the alteration features at Borup Fiord Pass as potentially habitable systems and astrobiological targets.

DATA AVAILABILITY STATEMENT

The raw data supporting the conclusion of this article will be made available by the authors, without undue reservation.

AUTHOR CONTRIBUTIONS

Field work was conducted by GL, CT, SG, JS, and AT. STXM was conducted by GL and JC. Sample preparation and analyses through Raman spectromicroscopy, XRD, and SEM were conducted by GL. The manuscript was primarily written by GL, with support and contributions from all other authors. All authors shared in data interpretation.

FUNDING

This research was funded by a grant from the NASA Exobiology and Evolutionary Biology Program (NNX13AJ32G) as well as from Department of Geological Sciences (Templeton funds) at the University of Colorado Boulder. GL was partially funded during a portion of this work by the National Science Foundation (NSF) Graduate Research Fellowship Program (GRFP) under Grant No. 2011123928. CT is currently supported through an ERC Synergy Grant (“DeepPurple” grant #856416) from the European Research Council (ERC). Field logistics and travel to/from Borup Fiord Pass were supported through Natural

REFERENCES

- Amils, R., González-Toril, E., Fernández-Remolar, D., Gómez, F., Aguilera, Á., Rodríguez, N., et al. (2007). Extreme Environments as Mars Terrestrial Analogs: The Rio Tinto Case. *Planet. Space Sci.* 55 (3), 370–381. doi:10.1016/j.pss.2006.02.006
- Amils, R. (2016). Lessons Learned from Thirty Years of Geomicrobiological Studies of Rio Tinto. *Res. Microbiol.* 167 (7), 539–545. doi:10.1016/j.resmic.2016.06.001
- Banfield, J. F., Bischoff, B. L., and Anderson, M. A. (1993). TiO₂ Accessory Minerals: Coarsening, and Transformation Kinetics in Pure and Doped Synthetic Nanocrystalline Materials. *Chem. Geol.* 110 (1–3), 211–231. doi:10.1016/0009-2541(93)00255-H
- Barnes, S. J., Holwell, D. A., and Le Vaillant, M. (2017). Magmatic Sulfide Ore Deposits. *Elements* 13 (2), 89–95. doi:10.2113/gselements.13.2.89
- Beegle, L. W., Bhartia, R., DeFlores, L. P., Asher, S. A., Burton, A. S., Clegg, S. M., et al. (2014). SHERLOC: Scanning Habitable Environments With Raman & Luminescence for Organics & Chemicals, an Investigation for 2020, Big Sky, MT, March 7–14, 2015 (San Francisco, CA: American Geophysical Union). Available at: <http://adsabs.harvard.edu/abs/2014AGUFM.P24A.06B>.
- Benzerara, K., Yoon, T. H., Tyliszczak, T., Constantz, B., Spormann, A. M., and Brown, G. E. (2004). Scanning Transmission X-ray Microscopy Study of Microbial Calcification. *Geobiology* 2 (4), 249–259. doi:10.1111/j.1472-4677.2004.00039.x
- Beysac, O., Goffé, B., Chopin, C., and Rouzaud, J. N. (2002). Raman Spectra of Carbonaceous Material in Metasediments: A New Geothermometer. *J. Metamorph. Geol.* 20 (9), 859–871. doi:10.1046/j.1525-1314.2002.00408.x
- Beysac, O., Goffé, B., Petitot, J.-P., Froigneux, E., Moreau, M., and Rouzaud, J.-N. (2003). On the Characterization of Disordered and Heterogeneous Carbonaceous Materials by Raman Spectroscopy. *Spectrochim. Acta A: Mol. Biomol. Spectrosc.* 59 (10), 2267–2276. doi:10.1016/S1386-1425(03)00070-2
- Bhartia, R., Beegle, L. W., DeFlores, L., Abbey, W., Razzell Hollis, J., Uckert, K., et al. (2021). Perseverance’s Scanning Habitable Environments with Raman and

Resources Canada’s (NRC) Polar Continental Shelf Program (PCSP). SEM/EDS measurements were conducted at the Nanomaterials Characterization Facility (NCF) at the University of Colorado Boulder. STXM measurements were performed at the Canadian Light Source, a national research facility of the University of Saskatchewan, which is supported by the Canada Foundation for Innovation (CFI), the Natural Sciences and Engineering Research Council (NSERC), the National Research Council (NRC), the Canadian Institutes of Health Research (CIHR), the Government of Saskatchewan, and the University of Saskatchewan.

ACKNOWLEDGMENTS

We thank Eric Ellison (CU Boulder) for advice and assistance in collecting and processing Raman microspectroscopy data. We thank Canadian Light Source staff scientist Dr. Jian Wang for his support. We also thank the Isotope Science Laboratory at the University of Calgary for EA-IRMS measurements.

SUPPLEMENTARY MATERIAL

The Supplementary Material for this article can be found online at: <https://www.frontiersin.org/articles/10.3389/fspas.2022.825019/full#supplementary-material>

- Luminescence for Organics and Chemicals (SHERLOC) Investigation. *Space Sci. Rev.* 217, 58. doi:10.1007/s11214-021-00812-z
- Bottrell, S. H., Newton, R. J., and Newton, R. J. (2006). Reconstruction of Changes in Global Sulfur Cycling from Marine Sulfate Isotopes. *Earth Sci. Rev.* 75, 59–83. doi:10.1016/j.earscirev.2005.10.004
- Brandes, J. A., Lee, C., Wakeham, S., Peterson, M., Jacobsen, C., Wirick, S., et al. (2004). Examining Marine Particulate Organic Matter at Sub-Micron Scales Using Scanning Transmission X-Ray Microscopy and Carbon X-Ray Absorption Near Edge Structure Spectroscopy. *Mar. Chem.* 92 (1–4), 107–121. doi:10.1016/j.marchem.2004.06.020
- Brolly, C., Parnell, J., and Bowden, S. (2016). Raman Spectroscopy: Caution When Interpreting Organic Carbon from Oxidising Environments. *Planet. Space Sci.* 121, 53–59. doi:10.1016/j.pss.2015.12.008
- Burns, R. G. (1987). “Gossans on Mars,” in Lunar and Planetary Science Conference, Proceedings (A89-10851 01-91), Houston, TX, March 16–20, 1987 (Cambridge and New York/Houston, TX: Cambridge University Press/Lunar and Planetary Institute), 713–721.
- Burns, R. G., and Fisher, D. S. (1990b). Evolution of Sulfide Mineralization on Mars. *J. Geophys. Res.* 95 (B9), 14169–14173. doi:10.1029/JB095iB09p14169
- Burns, R. G., and Fisher, D. S. (1990a). Iron-sulfur Mineralogy of Mars: Magmatic Evolution and Chemical Weathering Products. *J. Geophys. Res.* 95 (B9), 14415–14421. doi:10.1029/JB095iB09p14415
- Canfield, D. E. (2001). Biogeochemistry of Sulfur Isotopes. *Rev. Mineralogy Geochem.* 43 (1), 607–636. doi:10.2138/gsrmg.43.1.607
- Canfield, D. E., and Farquhar, J. (2012). “The Global Sulfur Cycle,” in *Fundamentals of Geobiology*. Editors A. H. Knoll, D. E. Canfield, and K. O. Konhauser (West Sussex: John Wiley & Sons), 49–64. doi:10.1002/9781118280874.ch5
- Chan, C. S., Fakra, S. C., Emerson, D., Fleming, E. J., and Edwards, K. J. (2010). Lithotrophic Iron-Oxidizing Bacteria Produce Organic Stalks to Control mineral Growth: Implications for Biosignature Formation. *Isme J.* 5 (4), 717–727. doi:10.1038/ismej.2010.173

- Cosmidis, J., Nims, C. W., Diercks, D., and Templeton, A. S. (2019). Formation and Stabilization of Elemental Sulfur through Organomineralization. *Geochim. Cosmochim. Acta* 247 (December), 59–82. doi:10.1016/j.gca.2018.12.025
- Cosmidis, J., and Templeton, A. S. (2016). Self-assembly of Biomorphic Carbon/sulfur Microstructures in Sulfidic Environments. *Nat. Commun.* 7, 12812. doi:10.1038/ncomms12812
- Davies, G. R., and Nassichuk, W. W. (1975). Subaqueous Evaporites of the Carboniferous Otto Fiord Formation, Canadian Arctic Archipelago: A Summary. *Geology* 3 (5), 273–278. doi:10.1130/0091-7613(1975)3<273:seotco>2.0.co;2
- Deegan, F. M., Troll, V. R., Bédard, J. H., Evenchick, C. A., Dewing, K., Grasby, S., et al. (2016). The Stiff Upper LIP: Investigating the High Arctic Large Igneous Province. *Geology Today* 32 (3), 92–98. doi:10.1111/gto.12138
- Edwards, K. J., Goebel, B. M., Rodgers, T. M., Schrenk, M. O., Gihring, T. M., Cardona, M. M., et al. (1999). Geomicrobiology of Pyrite (FeS₂) Dissolution: Case Study at Iron Mountain, California. *Geomicrobiol. J.* 16, 155–179. doi:10.1080/014904599270668
- Edwards, K. J., Hu, B., Hamers, R. J., and Banfield, J. F. (2000b). A New Look at Microbial Leaching Patterns on Sulfide Minerals. *FEMS Microbiol. Ecol.* 34 (3), 197–206. doi:10.1016/S0168-6496(00)0094-510.1111/j.1574-6941.2001.tb00770.x
- Edwards, K. J., Bond, P. L., Druschel, G. K., McGuire, M. M., Hamers, R. J., and Banfield, J. F. (2000a). Geochemical and Biological Aspects of Sulfide mineral Dissolution: Lessons from Iron Mountain, California. *Chem. Geology*. 169 (3–4), 383–397. doi:10.1016/S0009-2541(00)00216-3
- Ehlmann, B. L., and Edwards, C. S. (2014). Mineralogy of the Martian Surface. *Annu. Rev. Earth Planet. Sci.* 42 (1), 291–315. doi:10.1146/annurev-earth-060313-055024
- Embry, A., and Beauchamp, B. (2008). “Chapter 13 Sverdrup Basin,” in *Sedimentary Basins of the World*. Editors Andrew D. Miall (Amsterdam: Elsevier Science), 5, 451–471. doi:10.1016/S1874-5997(08)00013-0
- Evenchick, C. A., Davis, W. J., Bédard, J. H., Hayward, N., and Friedman, R. M. (2015). Evidence for Protracted High Arctic Large Igneous Province Magmatism in the Central Sverdrup Basin from Stratigraphy, Geochronology, and Paleodepths of Saucer-Shaped Sills. *Geol. Soc. Am. Bull.* 127 (9–10), 1366–1390. doi:10.1130/B31190.1
- Farley, K. A., Williford, K. H., Stack, K. M., Bhartia, R., Chen, A., de la Torre, M., et al. (2020). Mars 2020 Mission Overview. *Space Sci. Rev.* 216 (8), 41. doi:10.1007/s11214-020-00762-y
- Fernández-Remolar, D. C., Morris, R. V., Gruener, J. E., Amils, R., and Knoll, A. H. (2005). The Río Tinto Basin, Spain: Mineralogy, Sedimentary Geobiology, and Implications for Interpretation of Outcrop Rocks at Meridiani Planum, Mars. *Earth Planet. Sci. Lett.* 240 (1), 149–167. doi:10.1016/j.epsl.2005.09.043
- Ferrari, A. C., and Robertson, J. (2000). Interpretation of Raman Spectra of Disordered and Amorphous Carbon. *Phys. Rev. B* 61 (20), 14095–14107. doi:10.1103/PhysRevB.61.14095
- Fontboté, L., Kouzmanov, K., Chiaradia, M., and Pokrovski, G. S. (2017). Sulfide Minerals in Hydrothermal Deposits. *Elements* 13 (2), 97–103. doi:10.2113/gselements.13.2.97
- Gellert, R., and Clark, B. C. (2015). *In Situ* Compositional Measurements of Rocks and Soils with the Alpha Particle X-ray Spectrometer on NASA’s Mars Rovers. *Elements* 11 (1), 39–44. doi:10.2113/gselements.11.1.39
- Gleeson, D. F., Pappalardo, R. T., Anderson, M. S., Grasby, S. E., Mielke, R. E., Wright, K. E., et al. (2012). Biosignature Detection at an Arctic Analog to Europa. *Astrobiology* 12 (2), 135–150. doi:10.1089/ast.2010.0579
- Gleeson, D. F., Pappalardo, R. T., Grasby, S. E., Anderson, M. S., Beauchamp, B., Castaño, R., et al. (2010). Characterization of a Sulfur-Rich Arctic spring Site and Field Analog to Europa Using Hyperspectral Data. *Remote Sens. Environ.* 114 (6), 1297–1311. doi:10.1016/j.rse.2010.01.011
- Gleeson, D. F., Williamson, C., Grasby, S. E., Pappalardo, R. T., Spear, J. R., and Templeton, A. S. (2011). Low Temperature S₀ Biomineralization at a Supraglacial spring System in the Canadian High Arctic. *Geobiology* 9 (4), 360–375. doi:10.1111/j.1472-4669.2011.00283.x
- Grasby, S. E., Allen, C. C., Longazo, T. G., Lisle, J. T., Griffin, D. W., and Beauchamp, B. (2003). Supraglacial Sulfur Springs and Associated Biological Activity in the Canadian High Arctic-Signs of Life beneath the Ice. *Astrobiology* 3 (3), 583–596. doi:10.1089/153110703322610672
- Grasby, S. E., Beauchamp, B., and Bense, V. (2012). Sulfuric Acid Speleogenesis Associated with a Glacially Driven Groundwater System-Paleo-spring “Pipes” at Borup Fiord Pass, Nunavut. *Astrobiology* 12 (1), 19–28. doi:10.1089/ast.2011.0700
- Grasby, S. E., Percival, J. B., Bilot, I., Ardakani, O. H., Smith, I. R., Galloway, J., et al. (2022). Extensive Jarosite Deposits Formed through Auto-Combustion and Weathering of Pyritiferous Mudstone, Smoking Hills (Ingniryuat), Northwest Territories, Canadian Arctic - A Potential Mars Analogue. *Chem. Geol.* 587, 120634. doi:10.1016/j.chemgeo.2021.120634
- Hem, D. (1985). *Study and Interpretation the Chemical of Natural of Characteristics Water*. Reston: University Press of the Pacific. Available at: <http://pubs.usgs.gov/wsp/wsp2254/pdf/wsp2254a.pdf>.
- Hill, M. F. (2014). *Structure and Deformation at Borup Fiord Pass, NW Ellesmere Island, Arctic Canada and Insights to the Eurekan Orogeny*. Calgary: University of Calgary.
- Hitchcock, A. P. (2015). aXis2000 (Analysis of X-ray Images and Spectra) - is Free for Non-Commercial Use. Available at: <http://unicorn.mcmaster.ca/aXis2000.html> (last accessed 09 03, 2015).
- Hofmann, B. A., and Farmer, J. D. (2000). Filamentous Fabrics in Low-Temperature mineral Assemblages: Are They Fossil Biomarkers? Implications for the Search for a Subsurface Fossil Record on the Early Earth and Mars. *Planet. Space Sci.* 48, 1077–1086. doi:10.1016/S0032-0633(00)00081-7
- Hurowitz, J. A., Grotzinger, J. P., Fischer, W. W., McLennan, S. M., Milliken, R. E., Stein, N., et al. (2017). Redox Stratification of an Ancient lake in Gale Crater, Mars. *Science* 356 (6341). doi:10.1126/science.aah6849
- Jalilvand, F. (2006). Sulfur: Not a “Silent” Element Any More. *Chem. Soc. Rev.* 35 (12), 1256–1268. doi:10.1039/b417595f
- King, P. L., and McLennan, S. M. (2010). Sulfur on Mars. *Elements* 6 (2), 107–112. doi:10.2113/gselements.6.2.107
- Lafuente, B., Downs, R. T., Yang, H., and Stone, N. (2015). “1. The Power of Databases: The RRUFF Project,” in *Highlights in Mineralogical Crystallography*. Editors T. Armbruster and M. Danisi (Berlin, Germany: W. De Gruyter), 1–30. doi:10.1515/9783110417104-003
- Lau, G. E., Cosmidis, J., Grasby, S. E., Trivedi, C. B., Spear, J. R., and Templeton, A. S. (2017). Low-Temperature Formation and Stabilization of Rare Allotropes of Cyclooctasulfur (β-S₈ and γ-S₈) in the Presence of Organic Carbon at a Sulfur-Rich Glacial Site in the Canadian High Arctic. *Geochim. et Cosmochim. Acta* 200, 218–231. doi:10.1016/j.gca.2016.11.036
- Liu, X., Eusterhues, K., Thieme, J., Ciobota, V., Höschen, C., Mueller, C. W., et al. (2013). STXM and NanoSIMS Investigations on EPS Fractions before and after Adsorption to Goethite. *Environ. Sci. Technol.* 47 (7), 3158–3166. doi:10.1021/es3039505
- Machel, H. G. (2001). Bacterial and Thermochemical Sulfate Reduction in Diagenetic Settings - Old and New Insights. *Sediment. Geology*. 140, 143–175. doi:10.1016/S0037-0738(00)00176-7
- McCollom, T. M., and Hynnek, B. M. (2005). A Volcanic Environment for Bedrock Diagenesis at Meridiani Planum on Mars. *Nature* 438 (7071), 1129–1131. doi:10.1038/nature04390
- Ménez, B., Pasini, V., and Brunelli, D. (2012). Life in the Hydrated Suboceanic Mantle. *Nat. Geosci.* 5 (2), 133–137. doi:10.1038/ngeo1359
- Morris, R. V., Klingelhöfer, G., Schröder, C., Fleischer, I., Ming, D. W., Yen, A. S., et al. (2008). Iron Mineralogy and Aqueous Alteration from Husband Hill through Home Plate at Gusev Crater, Mars: Results from the Mössbauer Instrument on the Spirit Mars Exploration Rover. *J. Geophys. Res.* 113 (12). doi:10.1029/2008JE003201
- Naber, T. V., Grasby, S. E., Cuthbertson, J. P., Rayner, N., and Tegner, C. (2020). New Constraints on the Age, Geochemistry, and Environmental Impact of High Arctic Large Igneous Province Magmatism: Tracing the Extension of the Alpha Ridge onto Ellesmere Island. *Geol. Soc. Am. Bull.* doi:10.1130/B35792.1
- Nachon, M., Clegg, S. M., Mangold, N., Schröder, S., Kah, L. C., Dromart, G., et al. (2014). Calcium Sulfate Veins Characterized by ChemCam/Curiosity at Gale Crater, Mars. *J. Geophys. Res. Planets* 119 (9), 1991–2016. doi:10.1002/2013JE004588
- Percival, J. B., and Williamson, M.-C. (2016). Mineralogy and Spectral Signature of Reactive Gossans, Victoria Island, NT, Canada. *Appl. Clay Sci.* 119, 431–440. doi:10.1016/j.clay.2015.05.026
- Peretyazhko, T. S., Ming, D. W., Morris, R. V., Agresti, D. G., and Buckley, W. P. (2021). Formation of Fe(III) (Hydr)oxides from Fe(II) Sulfides: Implications for Akaganeite Detection on Mars. *ACS Earth Space Chem.* 5 (8), 1934–1947. doi:10.1021/acsearthspacechem.1c00075
- Peterson, R. C., Williamson, M.-C., and Rainbird, R. H. (2014). Gossan Hill, Victoria Island, Northwest Territories: An Analogue for Mine Waste Reactions

- within Permafrost and Implication for the Subsurface Mineralogy of Mars. *Earth Planet. Sci. Lett.* 400, 88–93. doi:10.1016/j.epsl.2014.05.010
- Picard, A., Gartman, A., and Girguis, P. R. (2016). What Do We Really Know About the Role of Microorganisms in Iron Sulfide mineral Formation? *Front. Earth Sci.* 4. doi:10.3389/feart.2016.00068
- Rampe, E. B., Ming, D. W., Blake, D. F., Bristow, T. F., Chipera, S. J., Grotzinger, J. P., et al. (2017). Mineralogy of an Ancient Lacustrine Mudstone Succession from the Murray Formation, Gale Crater, Mars. *Earth Planet. Sci. Lett.* 471, 172–185. doi:10.1016/j.epsl.2017.04.021
- Rapin, W., Meslin, P.-Y., Maurice, S., Vaniman, D., Nachon, M., Mangold, N., et al. (2016). Hydration State of Calcium Sulfates in Gale Crater, Mars: Identification of Bassanite Veins. *Earth Planet. Sci. Lett.* 452, 197–205. doi:10.1016/j.epsl.2016.07.045
- Rickard, D., and Luther, G. W. (2007). Chemistry of Iron Sulfides. *Chem. Rev.* 107, 514–562. doi:10.1021/cr0503658
- Rickard, D., Musmann, M., and Steadman, J. A. (2017). Sedimentary Sulfides. *Elements* 13 (2), 117–122. doi:10.1016/B978-0-444-52989-3.00014-3
- Rickard, D. (2012). *Sulfidic Sediments and Sedimentary Rocks* (Amsterdam: Elsevier Science). Available at: <https://books.google.com/books?hl=en&lr=&id=vkNseZ0SJKMC&oi=fnd&pg=PP1&dq=Sulfidic+sediments+and+sedimentary+rocks+&ots=9YG493pduN&sig=mUyRokaA6LAvnea9noijNUjpCQM#v=onepage&q=Sulfidic+sediments+and+sedimentary+rocks&f=false>
- Robertson, J., Ripley, E. M., Barnes, S., and Li, C. (2015). Sulfur Liberation From Country Rocks and Incorporation in Mafic Magmas. *Econ. Geol.* 110 (4), 1111–1123. doi:10.2113/econgeo.110.4.1111
- Rojas-Chapana, J. A., and Tributsch, H. (2004). Interfacial Activity and Leaching Patterns of *Leptospirillum ferrooxidans* on Pyrite. *FEMS Microbiol. Ecol.* 47 (1), 19–29. doi:10.1016/S0168-6496(03)00221-6
- Sadezky, A., Muckenhuber, H., Grothe, H., Niessner, R., and Pöschl, U. (2005). Raman Microspectroscopy of Soot and Related Carbonaceous Materials: Spectral Analysis and Structural Information. *Carbon* 43 (8), 1731–1742. doi:10.1016/j.carbon.2005.02.018
- Saumur, B. M., Dewing, K., and Williamson, M.-C. (2016). Architecture of the Canadian Portion of the High Arctic Large Igneous Province and Implications for Magmatic Ni-Cu Potential. *Can. J. Earth Sci.* 53 (March), 528–542. doi:10.1139/cjes-2015-0220
- Scheidegger, J. M., Bense, V. F., and Grasby, S. E. (2012). Transient Nature of Arctic Spring Systems Driven by Subglacial Meltwater. *Geophys. Res. Lett.* 39, L12405. doi:10.1029/2012GL051445
- Spötl, C., Houseknecht, W. D., and Jaques, R. C. (1998). Kerogen Maturation and Incipient Graphitization of Hydrocarbon Source Rocks in the Arkoma Basin, Oklahoma and Arkansas: A Combined Petrographic and Raman Spectrometric Study. *Org. Geochem.* 28 (9–10), 535–542. doi:10.1016/S0146-6380(98)00021-7
- Squyres, S. W., Aharonson, O., Clark, B. C., Cohen, B. A., Crumpler, L., De Souza, P. A., et al. (2007). Pyroclastic Activity at Home Plate in Gusev Crater, Mars. *Science* 316 (5825), 738–742. doi:10.1126/science.1139045
- Squyres, S. W., Arvidson, R. E., Bell, J. F., Calef, F., Clark, B. C., Cohen, B. A., et al. (2012). Ancient Impact and Aqueous Processes at Endeavour Crater, Mars. *Science* 336 (6081), 570–576. doi:10.1126/science.1220476
- Squyres, S. W., Grotzinger, J. P., Arvidson, R. E., Bell, J. F., Calvin, W., Christensen, P. R., et al. (2004). *In Situ* Evidence for an Ancient Aqueous Environment at Meridiani Planum, Mars. *Science* 306 (5702), 1709–1714. doi:10.1126/science.1104559
- Sumner, D. Y. (2004). Poor Preservation Potential of Organics in Meridiani Planum Hematite-Bearing Sedimentary Rocks. *J. Geophys. Res.* 109 (12), 1–8. doi:10.1029/2004JE002321
- Tarnas, J. D., Mustard, J. F., Sherwood Lollar, B., Stamenković, V., Cannon, K. M., Lorand, J.-P., et al. (2021). Earth-Like Habitable Environments in the Subsurface of Mars. *Astrobiology* 21 (6), 741–756. doi:10.1089/ast.2020.2386
- Taylor, G., and Eggleton, R. A. (2001). *Regolith Geology and Geomorphology*. West Sussex: Wiley. Available at: <https://books.google.com/books?id=5oErll55yacC>
- Taylor, K. G., and Konhauser, K. O. (2011). Iron in Earth Surface Systems: A Major Player in Chemical and Biological Processes. *Elements* 7 (2), 83–88. doi:10.2113/gselements.7.2.83
- Thode, H. G. (1991). “Sulphur Isotopes in Nature and the Environment: An Overview,” in *Stable Isotopes in the Assessment of Natural and Anthropogenic Sulphur in the Environment*-SCOPE. Editors H. R. Krouse and V. A. Grinenko (New York: John Wiley and Sons Ltd.), 1–26.
- Thorsteinsson, R., and Tozer, E. T. (1957). Geological Investigations in Ellesmere and Axel Heiberg Islands, 1956. *Arctic* 10 (1), 2–31. doi:10.14430/arctic3752
- Tilley, D. B., and Eggleton, R. A. (2005). Titanite Low-Temperature Alteration and Ti Mobility. *Clays Clay Miner.* 53 (1), 100–107. doi:10.1346/ccmn.2005.0530110
- Toulmin, P., III, Baird, A. K., Clark, B. C., Keil, K., Rose, H. J., Christian, R. P., et al. (1977). Geochemical and Mineralogical Interpretation of the Viking Inorganic Chemical Results. *J. Geophys. Res.* 82 (30), 4625–4634. doi:10.1029/J5082i028p04625
- Trivedi, C. B., Lau, G. E., Grasby, S. E., Templeton, A. S., and Spear, J. R. (2018). Low-Temperature Sulfidic-Ice Microbial Communities, Borup Fiord Pass, Canadian High Arctic. *Front. Microbiol.* 9 (JUL), 1–16. doi:10.3389/fmicb.2018.01622
- Trivedi, C. B., Stamps, B. W., Lau, G. E., Grasby, S. E., Templeton, A. S., and Spear, J. R. (2020). Microbial Metabolic Redundancy is a Key Mechanism in a Sulfur-Rich Glacial Ecosystem. doi:10.1128/mSystemsdoi:10.1128/mSystems.00504-20
- Vago, J. L., Westall, F., Coates, A. J., Jaumann, R., Korabely, O., Ciarletti, V., et al. (2017). Habitability on Early Mars and the Search for Biosignatures with the ExoMars Rover. *Astrobiology* 17, 471–510. doi:10.1089/ast.2016.1533
- Vaniman, D. T., Bish, D. L., Ming, D. W., Bristow, T. F., Morris, R. V., Blake, D. F., et al. (2014). Mineralogy of a Mudstone at Yellowknife Bay, Gale Crater, Mars. *Science* 343, 1243480–1243489. doi:10.1126/science.1243480
- Wallace, C. A., Spencer, R. J., Henderson, C. M., and Beauchamp, B. (1994). “The Lower Permian Mount Bayley Formation, Canadian Arctic: an Example of a Deep Subaqueous Evaporite,” in *Pangea: Global Environments and Resources*. Editors A. F. Embry, B. Beauchamp, and D. J. Glass (Calgary: Canadian Society of Petroleum Geologists), Memoir 17, 731–742.
- Wang, A., Bell, J. F., Li, R., Johnson, J. R., Farrand, W. H., Cloutis, E. A., et al. (2008). Light-Toned Salty Soils and Coexisting Si-Rich Species Discovered by the Mars Exploration Rover Spirit in Columbia Hills. *J. Geophys. Res.* 113 (12), 35. doi:10.1029/2008JE003126
- West, L., McGown, D. J., Onstott, T. C., Morris, R. V., Suchecki, P., and Pratt, L. M. (2009). High Lake Gossan Deposit: An Arctic Analogue for Ancient Martian Surficial Processes? *Planet. Space Sci.* 57 (11), 1302–1311. doi:10.1016/j.pss.2009.05.011
- Wong, G. M., Lewis, J. M. T., Knudson, C. A., Millan, M., McAdam, A. C., Eigenbrode, J. L., et al. (2020). Detection of Reduced Sulfur on Vera Rubin Ridge by Quadratic Discriminant Analysis of Volatiles Observed During Evolved Gas Analysis. *J. Geophys. Res. Planets* 125 (8), 1–19. doi:10.1029/2019JE006304
- Wright, K. E., Williamson, C., Grasby, S. E., Spear, J. R., and Templeton, A. S. (2013). Metagenomic Evidence for Sulfur Lithotrophy by Epsilonproteobacteria as the Major Energy Source for Primary Productivity in a Sub-aerial Arctic Glacial deposit, Borup Fiord Pass. *Front. Microbiol.* 4, 63. doi:10.3389/fmicb.2013.00063
- Zerkle, A. L., Farquhar, J., Johnston, D. T., Cox, R. P., and Canfield, D. E. (2009). Fractionation of Multiple Sulfur Isotopes during Phototrophic Oxidation of Sulfide and Elemental Sulfur by a green Sulfur Bacterium. *Geochim. Cosmochim. Acta* 73 (2), 291–306. doi:10.1016/J.GCA.2008.10.027
- Zolotov, M. Y., and Shock, E. L. (2003). Energy for Biologic Sulfate Reduction in a Hydrothermally Formed Ocean on Europa. *J. Geophys. Res.* 108 (E4), 5022. doi:10.1029/2002JE001966
- Zolotov, M. Y., and Shock, E. L. (2005). Formation of Jarosite-Bearing Deposits through Aqueous Oxidation of Pyrite at Meridiani Planum, Mars. *Geophys. Res. Lett.* 32 (21), 1–5. doi:10.1029/2005GL024253

Conflict of Interest: The authors declare that the research was conducted in the absence of any commercial or financial relationships that could be construed as a potential conflict of interest.

Publisher’s Note: All claims expressed in this article are solely those of the authors and do not necessarily represent those of their affiliated organizations, or those of the publisher, the editors and the reviewers. Any product that may be evaluated in this article, or claim that may be made by its manufacturer, is not guaranteed or endorsed by the publisher.

Copyright © 2022 Lau, Trivedi, Grasby, Spear, Cosmidis and Templeton. This is an open-access article distributed under the terms of the Creative Commons Attribution License (CC BY). The use, distribution or reproduction in other forums is permitted, provided the original author(s) and the copyright owner(s) are credited and that the original publication in this journal is cited, in accordance with accepted academic practice. No use, distribution or reproduction is permitted which does not comply with these terms.